

3rd International Symposium on Integrating CFD and Experiments in Aerodynamics  
20-21 June 2007  
U.S. Air Force Academy, CO, USA

## **Experimental and Numerical Investigation of Controlled, Small-Scale Motions in a Turbulent Shear Layer**

B. Vukasinovic\*  
A. Glezer\*  
Z. Rusak<sup>†</sup>

\*Woodruff School of Mechanical Engineering  
Georgia Institute of Technology  
Atlanta, GA 30332-0405  
bojan.vukasinovic@me.gatech.edu

<sup>†</sup>Department of Mechanical, Aerospace and Nuclear Engineering  
Rensselaer Polytechnic Institute  
Troy, NY 12180-3590

### **Abstract**

The effects of high-frequency fluidic actuation on the evolution of small- and large-scale motions in a turbulent shear layer downstream of a backward-facing step are investigated experimentally and numerically. The flow behind the step is characterized in the spatial and spectral domain by high-resolution diagnostic tools. Model stability problems with increasing complexity mimic the experimental setup and actuations and describe local and global flow behaviour. It is demonstrated that dissipative, high-frequency actuation effects the shear layer evolution through three domains: I – a localized dissipative, small scales domain having enhanced turbulent kinetic energy production and dissipation rate, II – a stabilized domain marked by concomitant suppression of turbulent kinetic energy production and dissipation rate, and III – a domain of re-emerging inviscid instability at lower natural frequencies and larger scales.

Keywords: shear layer stability, flow control, parabolic stability equations.

### **Introduction**

Direct small-scale (high-frequency) control has been extensively applied in the flow control applications where it was sought to effectively decouple the actuation input from the fundamental unstable frequencies of the base flow. Examples include control of the aerodynamic performance of bluff and streamlined bodies [1], and enhanced mixing in a plane [2] and axisymmetric [3] jets. These flow control applications were enabled by the introduction and characterization of synthetic jet actuators [4]. The previous investigations have demonstrated that high-frequency actuation has a profound impact on evolution of free- and wall-bounded turbulent shear flows even though the actuation is introduced locally at scales that are typically an order of magnitude smaller than the naturally dominant scales of the base flow. Wiltse & Glezer [2] indirectly estimated turbulent dissipation in the forced jet shear layer and concluded that even a small increase in velocity perturbations at high frequencies can lead to significant enhancement of dissipation, and consequently to a decrease in turbulent kinetic energy within the forced segment of the shear layer. Measurements in the near wake of a cylinder where the lift and drag are controlled by high-frequency surface actuation upstream of separation [5], showed a decrease in turbulent stresses in the forced shear layer accompanied by a decrease in vorticity, suggesting the increased dissipation in the near wake is a result of the forcing. The decrease of turbulent stresses as a result of high-frequency actuation was also observed in the wake of

| Report Documentation Page  |                                    |                                     |   | Form Approved<br>OMB No. 0704-0188       |                                 |
|--|------------------------------------|-------------------------------------|---|--|---------------------------------|
| Public reporting burden for the collection of information is estimated to average 1 hour per response, including the time for reviewing instructions, searching existing data sources, gathering and maintaining the data needed, and completing and reviewing the collection of information. Send comments regarding this burden estimate or any other aspect of this collection of information, including suggestions for reducing this burden, to Washington Headquarters Services, Directorate for Information Operations and Reports, 1215 Jefferson Davis Highway, Suite 1204, Arlington VA 22202-4302. Respondents should be aware that notwithstanding any other provision of law, no person shall be subject to a penalty for failing to comply with a collection of information if it does not display a currently valid OMB control number. |                                    |                                     |   |  |                                 |
| 1. REPORT DATE<br><b>JUN 2007</b>  |                                    | 2. REPORT TYPE<br><b>N/A</b>        |   | 3. DATES COVERED<br><b>-</b>             |                                 |
| 4. TITLE AND SUBTITLE<br><b>Experimental and Numerical Investigation of Controlled, Small-Scale Motions in a Turbulent Shear Layer</b>   |                                    |                                     |   | 5a. CONTRACT NUMBER                      |                                 |
|  |                                    |                                     |   | 5b. GRANT NUMBER                         |                                 |
|  |                                    |                                     |   | 5c. PROGRAM ELEMENT NUMBER               |                                 |
| 6. AUTHOR(S)   |                                    |                                     |   | 5d. PROJECT NUMBER                       |                                 |
|  |                                    |                                     |   | 5e. TASK NUMBER                          |                                 |
|  |                                    |                                     |   | 5f. WORK UNIT NUMBER                     |                                 |
| 7. PERFORMING ORGANIZATION NAME(S) AND ADDRESS(ES)<br><b>Georgia Institute of Technology Atlanta, GA 30332-0405</b>  |                                    |                                     |   | 8. PERFORMING ORGANIZATION REPORT NUMBER |                                 |
| 9. SPONSORING/MONITORING AGENCY NAME(S) AND ADDRESS(ES)  |                                    |                                     |   | 10. SPONSOR/MONITOR'S ACRONYM(S)         |                                 |
|  |                                    |                                     |   | 11. SPONSOR/MONITOR'S REPORT NUMBER(S)   |                                 |
| 12. DISTRIBUTION/AVAILABILITY STATEMENT<br><b>Approved for public release, distribution unlimited</b>  |                                    |                                     |   |  |                                 |
| 13. SUPPLEMENTARY NOTES<br><b>Third International Symposium on Integrating CFD and Experiments in Aerodynamics, June 20-21, 2007, The original document contains color images.</b>   |                                    |                                     |   |  |                                 |
| 14. ABSTRACT   |                                    |                                     |   |  |                                 |
| 15. SUBJECT TERMS  |                                    |                                     |   |  |                                 |
| 16. SECURITY CLASSIFICATION OF:  |                                    |                                     | 17. LIMITATION OF ABSTRACT<br><b>UU</b> | 18. NUMBER OF PAGES<br><b>47</b>         | 19a. NAME OF RESPONSIBLE PERSON |
| a. REPORT<br><b>unclassified</b>   | b. ABSTRACT<br><b>unclassified</b> | c. THIS PAGE<br><b>unclassified</b> |   |  |                                 |

an airfoil [6] and was attributed to the increased dissipation and a decrease of energy transfer from the free stream. Cain et al. [7] performed a numerical study of high-frequency forcing on a free shear layer and concluded that the reduction in turbulent kinetic energy in the forced flow results from simultaneous increase of the dissipation rate of turbulent kinetic energy and decrease in its production rate. The efficacy of control approach at frequencies substantially higher than the naturally-evolving flow frequencies was also demonstrated in the reduction of jet noise [8], cavity noise [9], and mitigation of optical effects during in-flight optical transmission [10]. Simulations of cavity flow with the control by vortex shedding from the cylinder showed significant flow stabilization at  $M = 0.6$  [11]. Shaw et al. [12] recently demonstrated suppression of pressure fluctuations in flight conditions up to  $M = 0.85$  by the application of synthetic jet, high-frequency control. Numerical simulations [13] showed significant impact of direct high-frequency excitation on the suppression of cavity modes at  $M = 1.19$ . Therefore, there is a solid body of evidence of the significant effects that this control approach has on the ensuing flow field. However, there is still no unified understanding about the mechanisms by which the effected small-scale control alters the baseline flow. Wiltse & Glezer [2] showed that direct addition of high-frequency energy into the shear layer alters the energy cascade across broadband range and postulated that enhanced energy transfer from large to small scales may be the driving mechanism. Next mechanism for explaining the effects of high-frequency forcing was proposed by Stanek et al. [14, 15], who hypothesized that high-frequency excitation modifies the time-averaged velocity distributions within the baseline shear layer and thereby makes it stable to low-frequency perturbations. This model implies that stability analyses based on linear or nonlinear models can be used to describe high-frequency excitation in a similar manner that has been used for low-frequency excitation. In fact, an attractive feature of this approach is that a single stability analysis technique can be used in principle across a range of low and high frequencies to describe the control of shear layers.

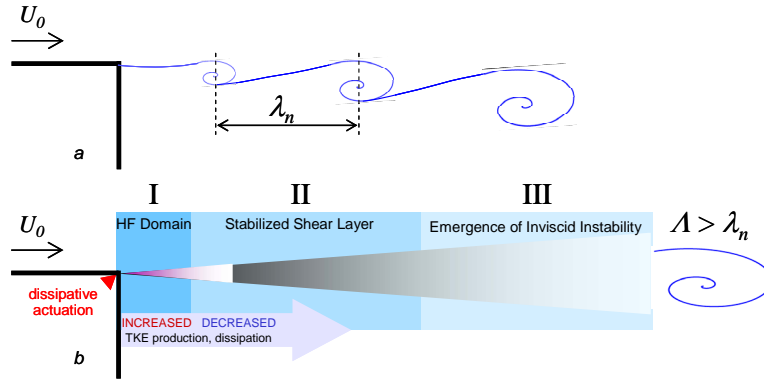


**Figure 1. Schematics of the effect of dissipative, high-frequency actuation on shear layer evolution denoted through three domains: I – localized dissipative (HF) domain having enhanced TKE production and dissipation rate, II – stabilized domain marked by concomitant suppression of TKE production and dissipation rate, and III – domain of re-emerging inviscid instability.**

The present work aims at extending the insight into the mechanisms and effects of dissipative, small-scale actuation of the shear layer, which can be outlined in the schematics shown in Fig. 1. Figure 1a describes the growth of perturbations in the free shear layer. As the direct, small-scale control is applied, there is a localized interaction domain extending in the downstream direction (Fig. 1b). It is denoted as Domain I, and is characterized by dominant signatures of the high-frequency actuation: enhanced dissipation and production of turbulent kinetic energy. As a consequence, baseline flow is altered in such a way that it is no longer unstable to the natural frequency of the non-actuated flow. This spatial domain is denoted as Domain II, and can be viewed as the “stabilized” shear layer having reduced production of turbulent kinetic energy and overall turbulent intensity. Ultimately, altered baseline flow starts to develop a new inviscid instability in Domain III. This instability is governed by the local shear layer properties, and thereby is characterized by a lower frequency than that dominating the original baseline flow. The present research is comprised on an integrated experimental and numerical/theoretical work, with the emphasis on high temporal resolution in the constrained spatial domain (Domain I and partially Domain II) of the former, and lower temporal resolution analysis over a full spatial span (Domains II through III) of the latter. This paper focuses

on an investigation of the role and coupling mechanisms of high-frequency forcing in the local and global evolution of a plane turbulent shear layer. The main objectives are to gain a better integrated experimental and theoretical understanding of the role of the actuation in the enhancement of near field mixing and its effect on suppression of large-scale coherent motions.

## Experimental Setup and Flow Diagnostics

The experimental investigation is conducted in a low-speed, closed return wind tunnel at Georgia Tech that is specifically designed for high-resolution PIV measurements. The tunnel test section has transparent walls on three sides and measures  $25.4 \times 40.6 \times 132.1$  cm. The tunnel screens are removed and a number of honeycomb sections is reduced to avoid PIV seeding blockage and accumulation. Nonetheless, the measured free stream turbulence intensity is less than 0.5% over the entire range of tunnel speeds. The shear layer is generated by the flow separation off the edge of a backward-facing step, thus representing a canonical single-stream shear flow. This flow configuration is selected not only because of its inherent affinity for numerical studies, but because it also forces a sudden flow separation owing a steep change in the flow geometry. The step spans the full width of the test section and its height relative to the wall of the test section is  $H = 50.8$  mm. Although the step is built in the upper wall of the test section (Figure 2a), all results are presented in a flipped field of view. The actuation is effected by six synthetic jet actuator modules integrated into the step surface, which span about 95% of the step width. The boundary layer over the step surface is tripped well upstream of the edge, and the flow over the actuators is turbulent. In the absence of actuation, the boundary layer thickness at the step edge is  $\delta_0 = 4.7$  mm, the momentum thickness is  $\theta_0 = 0.35$  mm, at the Reynolds number  $Re_H \approx 43,000$  (based on the step height  $H$  and the free stream velocity  $U_0$ ) and  $Re_{\theta_0} \approx 312$ . The boundary layer shape factor at the step edge is  $h_0 = 1.4$ .

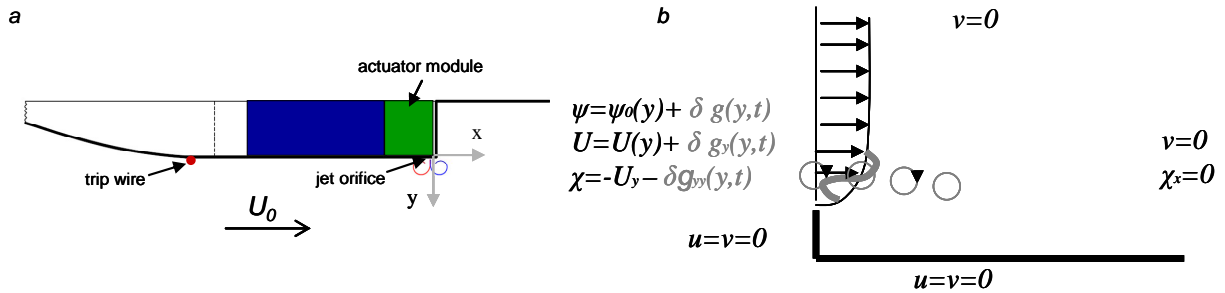


Figure 2. Schematics of the flow geometry (a) and mathematical model (b).

Each actuator module is individually-addressable and issues a synthetic jet through two orifices that measure  $0.38 \times 18.3$  mm, having the spanwise spacing 1.9 mm between them. The actuator orifices are located 8 mm (21 orifice widths) upstream of the step edge and the jets issue normal to the step surface. Figure 2a shows the schematics of flow geometry. The input to the actuators is a sinusoidal voltage signal of prescribed frequency. Each module is calibrated outside of the test section by measuring cross stream velocity distributions over the exit orifice using hot wire anemometry, and the average exit jet velocity  $U_j$  is defined as an average over the expulsion part of the actuation cycle. A movable miniature pressure probe is used for assessing the module performance in-situ between the runs. The operating frequency of the actuators is within the range  $St_H = 2.2 - 8.1$  for the nominal free stream flow, and as a representative for the small-scale (high-frequency) actuation, nominal operating frequency is set at  $f_d = 2000$  Hz ( $St_H = 7.36$ ). The jet momentum coefficient defines a relative jet “strength” as a ratio of the jet and the free-stream momentums  $C_\mu = U_j^2 b_j / (U_0^2 H)$ , where  $b_j = 0.38$  mm is the orifice width. To assess the effect of the jet momentum coefficient on the flow evolution, it is varied between  $C_\mu = 0.004$  and  $0.051$  in the present work.

The flow fields are characterized by the particle image velocimetry (PIV) in spatial and hot wire anemometry in spectral domain. Default spatial PIV domain consists of eleven partially overlapping windows spanning  $-0.5 < y/H < 0.5$  and  $-0.5 < x/H < 2.5$  (in the vertical,  $x$ - $y$ , plane, c.f. Figure 2a) with the imaging resolution of  $26.9 \mu\text{m}/\text{pixel}$ . Highly-resolved measurements of the turbulent dissipation rate and interaction between the high-frequency vortex

pairs and the cross flow are taken at finer resolution, down to 6.5  $\mu\text{m}/\text{pixel}$ . For the flow mapping, both the CCD camera and part of the laser-sheet optics are positioned by the computer-controlled traverse mechanisms. Initial processing of the PIV data is done by commercial Insight software, while the data postprocessing is done by the custom-developed software at Georgia Tech, including the composition of individual measurement windows into the single output domain. Spectral characterization of the flow is done using a DISA anemometer with a single-sensor miniature probe. Hot wire measurements are taken across the shear layer at eight downstream locations  $x/H = 0.1, 0.2, 0.4, 0.6, 0.8, 1, 1.18, \text{ and } 1.38$ .

## Mathematical Model

A two-dimensional, unsteady, incompressible, viscous flow around a backward facing step of height  $H$  with far-field speed  $U_0$  is considered (see Fig. 2b). Distances are scaled with  $H$  and speeds with  $U_0$ . The flow is described by the Navier-Stokes equations in the vorticity and stream function formulation:

$$\begin{aligned}\chi_t + \psi_y \chi_x - \psi_x \chi_y &= \frac{1}{\text{Re}} (\chi_{xx} + \chi_{yy}), \\ \chi &= -(\psi_{xx} + \psi_{yy}).\end{aligned}\tag{1}$$

Here  $\psi(x,y,t)$  is the stream function and  $\chi(x,y,t)$  is the vorticity. The flow axial and transverse speed components are given by  $u = \psi_y$ ,  $v = -\psi_x$  and the Reynolds number is  $\text{Re} = \rho U H / \mu$ , where  $\rho$  is the flow constant density and  $\mu$  is the flow constant viscosity. We assume a high Reynolds number flow,  $\text{Re} \gg 1$ . The flow is subjected to the following boundary conditions. Along the inlet section at  $x=0$  and  $y>0$  we prescribe for all time  $t>0$  the incoming stream function and the vorticity as follows:

$$\begin{aligned}\psi(0, y, t) &= \psi_0(y) + \delta g(y, t), \\ \chi(0, y, t) &= -\psi_{0yy} - \delta g_{yy}(y, t).\end{aligned}\tag{2}$$

Here,  $\psi_0(y)$  describes the inlet base volumetric flux, resulting in a base incoming axial speed profile  $U_0(y) = \psi_{0y}$  where it is zero at  $y=0$  and tends to one as  $y$  increases. This base speed profile is perturbed by an upstream flux perturbation of given size  $\delta$  and general shape  $g(y,t)$ , where typically,  $0 < \delta < 1$ ,  $g(0,t)=0$ , and  $g$  tends to zero as  $y$  increases. Along the step walls the no penetration and no slip conditions are set. As  $y$  increases the transverse speed approaches zero. Also, as  $x$  increases the transverse speed and vorticity axial gradients approach zero. The flow is governed by two parameters  $1/\text{Re}$  and  $\delta$ . When these parameters are sufficiently small it may be amenable to asymptotic analysis. In the following sections we describe the development of a set of theoretical stability studies with increasing complexity which support each other, mathematically mimic the experimental setup (Fig. 2a), shed light on the measured data, and explore the possible interacting mechanisms of upstream excitation at low and high frequencies.

## Linear Stability Studies

The computed base states with  $\delta=0$  at high Reynolds numbers exhibit in most of the domain away from the step that the local flow is nearly parallel, i.e. the transverse speed is near zero. Let the perturbation's stream function be locally given by  $\psi_1(x, y, t) = \phi(y) \exp[i(\alpha x - \omega t)]$  where  $\alpha$  and  $\omega$  are the perturbation's wave number and frequency. The function  $\phi(y)$  is described by Rayleigh eigenvalue problem at every axial position:

$$L(\phi) = (U(x, y)\alpha - \omega)(\phi_{yy} - \alpha^2 \phi) - \alpha U_{yy}(x, y)\phi + \frac{i}{\text{Re}}(\phi_{yyy} - 2\alpha^2 \phi_{yy} + \alpha^4 \phi) = 0, \text{ as } |y| \rightarrow \infty, \phi \rightarrow 0. \tag{3}$$

When temporal stability is studied, the wave number  $\alpha$  is real and given and we look for the complex eigenvalues  $\omega_R + i\omega_I$  and related eigenfunctions of (3). When spatial stability is investigated, the frequency  $\omega$  is real and given and we look for the complex eigenvalues  $\alpha_R + i\alpha_I$  and related eigenfunctions of (3). Here  $\omega_R$  is the

frequency of oscillations and  $\omega_I$  is the temporal growth rate of the perturbation,  $\alpha_R$  is the wave number periodicity, and  $\alpha_I$  is the spatial expansion rate of the perturbation. The local natural frequency  $f_n$  at each  $x$  is found from the frequency  $\omega_R$  for which the growth rate is maximal and perturbation is most amplified.

To improve on the predictions of the local stability analysis, the following asymptotic investigation is conducted. We assume that the base flow is nearly parallel, i.e. the flow develops over a longer axial distance than the transverse distance  $u=O(1)$  and  $v=O(\varepsilon)$ ,  $|\varepsilon| \ll 1$ . Here  $\varepsilon = H/l_s$  where  $l_s$  is the length of the separation zone. Then,  $u = U(\tilde{x}, y)$ ,  $v = \varepsilon V(\tilde{x}, y)$  where  $\tilde{x} = \varepsilon x$ . Following Gaster et al. [16] it can be shown that

$$\psi_1 = A(\tilde{x}, \omega) \exp \left[ \int_0^{\tilde{x}} \alpha_I(\tilde{x}', \omega) d\tilde{x}' \right] \times \sqrt{\phi_R^2(\tilde{x}, y, \omega) + \phi_I^2(\tilde{x}, y, \omega)} \times \sin \left( \omega t - \int_0^{\tilde{x}} \alpha_I(\tilde{x}', \omega) d\tilde{x}' + \phi(\tilde{x}, y, \omega) \right) \quad (4)$$

where at each  $x$  the eigenvalues  $\alpha_R(\tilde{x}, \omega) + i\alpha_I(\tilde{x}, \omega)$  and eigenfunctions  $\phi(\tilde{x}, y, \omega) = \phi_R(\tilde{x}, y, \omega) + i\phi_I(\tilde{x}, y, \omega)$  are solved from (3) for a given  $\omega$ . Amplitude  $A(\tilde{x}, \omega)$  is described the solvability condition of the second-order

problem,  $A_{\tilde{x}} + qA = 0$ ,  $A(0) = 1$  where  $q(\tilde{x}, \omega) = \int_{-1}^{\infty} b(\tilde{x}, \omega) \bar{\phi}(\tilde{x}, y, \omega) dy / \int_{-1}^{\infty} a(\tilde{x}, \omega) \bar{\phi}(\tilde{x}, y, \omega) dy$ ,  $\bar{\phi}(\tilde{x}, y, \omega)$  is the

adjoint function of  $\phi(\tilde{x}, y, \omega)$ , and  $a = 2\omega\alpha\phi + U(\phi_{yy} - 3\alpha^2\phi) - U_{yy}\phi$

$$b = \omega(\alpha_x\phi + 2\alpha\phi_x) + U(\phi_{yyx} - 3\alpha^2\phi_x - 3\alpha\alpha_x\phi) - U_{yy}\phi_x + V(\phi_{yyy} - \alpha^2\phi_y) - V_{yy}\phi_y.$$

Equation (4) provides insight into the development of the perturbations in space. The square root and sin terms in (4) describe a periodic street of vortices with a variable wave-length. The first two terms in (4) describe the perturbation's amplitude along the shear layer. At a low frequency of the upstream actuation, there are two opposing effects along the axial direction: 1) the near-field behaviour where the given excitation frequency is less than twice the natural frequency at that position. There,  $\alpha_I > 0$ , the term  $\exp[\int_0^{\tilde{x}} \alpha_I(\tilde{x}', \omega) d\tilde{x}']$  grows with  $x$ , while

$A \sim 1$ . Therefore, the perturbation amplitude grows in the near field over a distance from the step. This distance is related to position where the imposed frequency matches twice the local base flow natural frequency; 2) the downstream mid-field behaviour where the given excitation frequency is greater than twice the natural frequency at that position. There,  $\alpha_I = 0$ , the integral term is constant, and  $A$  decays exponentially with  $x$ . Therefore, in the mid field, the perturbation decays with distance from the step. Yet, it is expected that the perturbation feeds energy to the global mode that dominates the base flow at distances far from the step. A schematic description of this behaviour at a low excitation frequency is shown in Fig. 3a. Moreover, it is also predicted that the position where perturbation amplitude is maximum shifts toward the step as actuation frequency grows. On the other hand, when excitation frequency is greater than twice the maximum natural frequency along the shear layer,  $\alpha_I = 0$  all along the layer, the

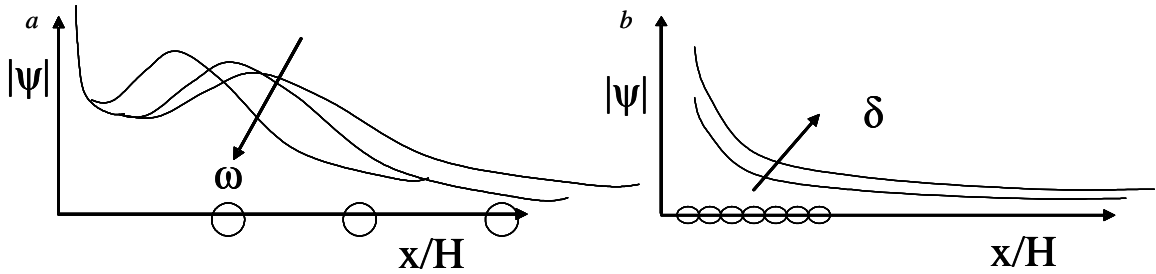


**Figure 3. Schematic description of perturbation's amplitude with the increase in excitation frequency for a low-frequency excitation (a) and with an increase in excitation amplitude for a high-frequency excitation (b).**

near-field behaviour is suppressed, and the perturbation's size only decays with distance from the step (Fig. 3b), feeding less energy to the global mode that dominates the flow at large distances from the step. It is also clear that the perturbations' strength increases with the increase of excitation amplitude  $\delta$ . Figures 3a and b support the flow description suggested in Fig. 1.

## Nonlinear Parabolic Stability Equations

The nonlinear parabolic stability equation (NPSE) approach extends the local linear stability problem (3) and the second-order model equation (4). The perturbation's stream function is given by

$$\psi_1(x, y, t) = \sum_{m=-M}^M \varepsilon_{m0} \phi_m(x, y) \exp \left[ \int_0^x a_m(x') dx' - im\omega_0 t \right] \text{ where } \omega_0 \text{ is a fundamental frequency, } m \text{ is the mode}$$

index,  $a_m(x)$  is the mode wave number,  $\phi_m(x, y)$  is the mode shape function, and  $\varepsilon_{m0}$  is the perturbation amplitude at  $x=0$  and is usually a small number in its size. The vorticity perturbation is:

$$\chi_1(x, y, t) = \sum_{m=-M}^M \varepsilon_{m0} \tilde{\chi}_m(x, y) \exp \left[ \int_0^x a_m(x') dx' - im\omega_0 t \right], \quad \tilde{\chi}_m(x, y) = - \left( \phi_m a_m^2 + \phi_{myy} + 2\phi_{mx} a_m + \phi_m a_{mx} \right). \text{ The}$$

upstream, wall, and far-field conditions, for all  $m$ , are  $\phi_m(0, y) = \phi_{m0}$ ,  $a_m(0) = a_{m0}$ ,  $\phi_m(x, -1) = 0$ ,  $\phi_{my}(x, -1) = 0$ ,  $\phi_m(x, y \rightarrow \infty) = 0$ ,  $\phi_{my}(x, y \rightarrow \infty) = 0$ . The modes' shape functions are solved by a system of  $2M+1$  coupled nonlinear parabolic equations, each of the form:

$$\begin{aligned} \varepsilon_{m0} \left\{ L_0(\phi_m, \tilde{\chi}_m) + L_1(\phi_{mx}, \tilde{\chi}_{mx}) + L_2(\phi_m, \tilde{\chi}_m) a_{mx} + L_3(\phi_{my}, \tilde{\chi}_{my}) \right\} = \\ \sum_{k=-M}^{M-1} \varepsilon_{k0} \varepsilon_{l0} \left[ a_k \phi_k \left( \tilde{\chi}_{ly} - 2a_l \phi_{lxy} \right) + \phi_{kx} \left( \tilde{\chi}_{ly} + 2a_k^2 \phi_{ly} \right) - \left( \tilde{\chi}_{kx} + a_k \tilde{\chi}_k - a_k (a_{kx} - a_{lx}) \phi_k \right) \phi_{ly} \right] \\ l=m-k \\ \times \exp \left[ \int_0^x (a_k + a_l - a_m) dx' \right] \quad \text{where} \quad \tilde{\chi}_m = - \left( a_m^2 \phi_m + \phi_{myy} \right) \end{aligned} \quad (5)$$

where

$$\begin{aligned} \tilde{\chi}_m = - \left( a_m^2 \phi_m + \phi_{myy} \right), \quad L_0(\phi_m, \tilde{\chi}_m) = \left( \Psi_y a_m - im\omega_0 - \frac{a_m^2}{\text{Re}} \right) \tilde{\chi}_m + \Psi_{yyy} a_m \phi_m - \frac{1}{\text{Re}} \tilde{\chi}_{myy}, \\ L_1(\phi_{mx}, \tilde{\chi}_{mx}) = \left( \Psi_y - \frac{4a_m}{\text{Re}} \right) \tilde{\chi}_{mx} + \left( \Psi_{yyy} + 2im\omega_0 a_m - 2a_m^2 \Psi_y \right) \phi_{mx}, \\ L_2(\phi_m, \tilde{\chi}_m) = - \frac{2}{\text{Re}} \tilde{\chi}_m - \left( \Psi_y a_m - im\omega_0 + \frac{4a_m^2}{\text{Re}} \right) \phi_m, \quad L_3(\phi_{my}, \tilde{\chi}_{my}) = - \Psi_x \tilde{\chi}_{my} - \Psi_{yyx} \phi_{my}. \end{aligned}$$

The right hand side of (5) allows for the nonlinear interaction between the various modes assigned and cascade of energy from low to high frequencies. Also, the equation for  $m=0$  gives the steady distortion mode of the base flow due the nonlinear interaction between all the other perturbation modes. The base flow plus the zero mode give the mean flow. A numerical code has been developed to solve the problem (5). Following Day et al. [17], the code uses the finite-differences method with first-order backward differencing in the  $x$ -direction and second-order central differencing in the  $y$ -direction. The resulting scheme for each equation is

$$\left[ R_m^{i+1} \Delta x + Q_m^{i+1} \right] X_m^{i+1} = Q_m^{i+1} X_m^i + N_m^{i+1} \text{ where } X^i = \left[ \dots \tilde{\chi}_m^i, \phi_m^i, \dots \right]^T \text{ and } N_m^{i+1} \text{ results from the}$$

nonlinear terms in  $N$ . The solution of these equations requires sub iterations until convergence at each axial location  $i$  is achieved. Again, the numerical experience shows that for numerical stability the vertical step size  $\Delta y$  must obey,

$\Delta y / \Delta x < 0.25$ . Also, relatively small initial amplitudes  $\varepsilon_{m0}$  are needed for achieving convergence of the solution

over a large distance along the shear layer. In solving these equations, the values of  $a_m(x)$  for each mode  $-M \leq m \leq M$  need to be updated due to the perturbed nature of the flow at each axial location  $i$ . They are integrated using an iterative strategy according to the following formula of Day et al. [17]

$$a_{m,i+1}^{n+1} = a_{m,i+1}^n + (\sigma_m / \Delta x) \left[ \int_{-\infty}^{+\infty} \left( \bar{v}_{m,i+1}^n \right)^\dagger \left( \bar{v}_{m,i+1}^n - \bar{v}_{m,i}^n \right) dy \right] / \left[ \int_{-\infty}^{+\infty} \left| \bar{v}_{m,i+1}^n \right|^2 dy \right]. \text{ Here, } n \text{ is the iteration step}$$

number and  $\bar{v}_{m,i}^n$  is the velocity vector shape function of mode  $m$  at location  $i$  and iteration  $n$ . Also,  $\sigma_m$  is a convergence control factor of mode  $m$  and is determined by matching the NPSE results for very small values of  $\varepsilon_{m0}$  with the results for a linear analysis.

## Baseline Flow

The baseline flow at  $Re=43,000$  in the absence of actuation is first characterized experimentally in both spatial and spectral domains. Figure 4a shows the ensemble-averaged composite flow field measured by the PIV in terms of the raster plot of the spanwise vorticity with overlaid equidistant mean velocity profiles. As the oncoming boundary layer terminates into the single-stream shear layer at the sharp flow separation at the edge, there is an asymmetry in its cross-stream spreading owing to the strong entrainment on the low-speed (wall) side. As a result, the shear layer spreading is biased towards the wall, and the mean flow evolves slowly in the downstream direction. The momentum thickness  $\theta$  of the shear layer increases linearly in the downstream direction. The baseline flow is evidently not self-similar in the measured near field, while the flow self similarity in the far field is not expected because of the finite height of the step, i.e., proximity of the wall boundary. In order to conduct a relevant linear and nonlinear stability analysis of the experimental shear layer behind a backward facing step at  $Re=43,000$ , a baseline flow field was computed numerically using the Fluent code with the  $k-\varepsilon$  model for turbulence in the domain  $-1 < y/H < 5$  and  $-5 < x/H < 20$ . It is found that the computed mean velocity profiles are similar to the measured mean profiles in the entire domain  $0 < x/H < 2.5$ . Figure 4b shows the similarity of the computed mean flow vorticity field with the experimental measurements in Fig. 4a. Figure 4c shows the flow streamlines in the full numerical domain. The baseline flow reattaches at  $x/H \sim 5.5$ .

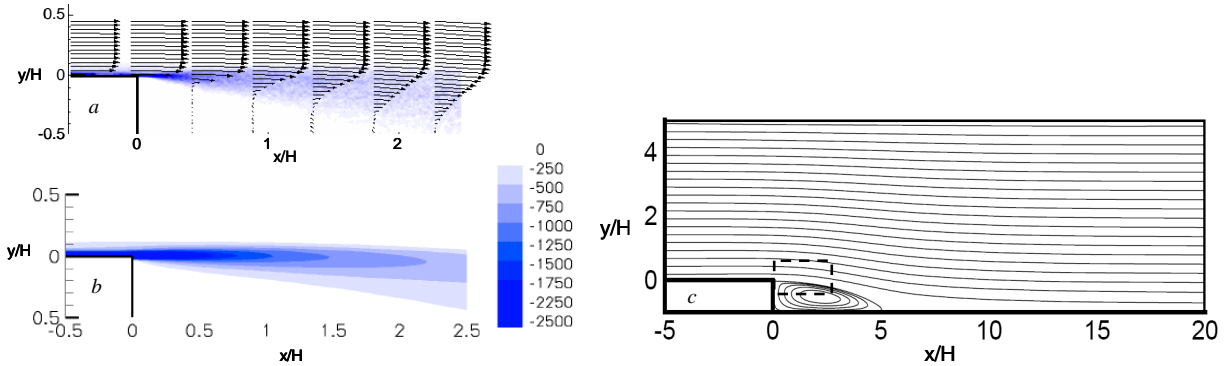


**Figure 4. Measured ensemble-averaged vorticity  $\zeta_z$  field with overlaid mean velocity profiles (a), computed mean vorticity field (b) and streamlines over the full computation domain (c).**

To further investigate natural receptivity to disturbances of the baseline shear layer, spectral analysis of the baseline flow is done using hot-wire anemometry (HWA). For that purpose, power spectra of the velocity fluctuations in the baseline flow are measured across the shear layer at eight downstream locations through  $x/H = 1.4$ . It should be emphasized that no source of disturbance is applied to the flow, i.e., all disturbances that are amplified by the flow, which energy content is measured by the HWA, originate from the ambient noise. Figure 5a shows contour plots of the extracted energy content from power spectra measurements at frequency  $f = 300$  Hz, which is estimated to be within the receptivity range of the baseline flow. Three additional power spectra fields are also analyzed at



frequencies 200, 100, and 50 Hz (not shown). As expected, the domains of peak amplification of energy content move downstream with the decrease in frequency. As seen in Fig. 5a, fluid motions at 300 Hz are the most amplified around  $x/H = 0.4$  ( $x/\theta_0 \approx 60$ ). Energy content at 200 Hz peaks at about  $x/H = 0.6$  ( $x/\theta_0 \approx 90$ ), while the maximum amplification of motions at lower frequencies appear to peak outside of the measurement domain. As also marked on Fig. 5a, each contour plot of energy content yields the location of maximum amplification along with the estimate of its upstream and downstream spatial boundaries. Spatial locations of the peak energy content at the analyzed frequencies are plotted in Fig. 5b, along with the most amplified frequency  $f_n$  resulting from the local stability analysis of the mean flow field using Rayleigh's equation (3). The nominal line represents the axial position of the middle of a domain with a certain dominant frequency, the lower bound represents the most upstream axial location of this domain and the upper bound is the most downstream axial location of this domain. It can be seen that the natural frequency decreases with distance from the step, indicating the growth of the shear layer thickness with distance, as is found from the mean flow profiles. Note that some experimental data do not yield all boundaries due to the limited measurement domain, and only the lower boundary profile is complete for all frequencies. Overall agreement between the measurements of the peak energy content and the computed most amplified frequency is good, although the linear stability analysis results tend to align better with the lower boundary of the experimental data. Also note that the naturally most amplified frequency decreases with the growth of  $\theta$  such that  $St_\theta = f_n \theta/U \sim 0.032$ .

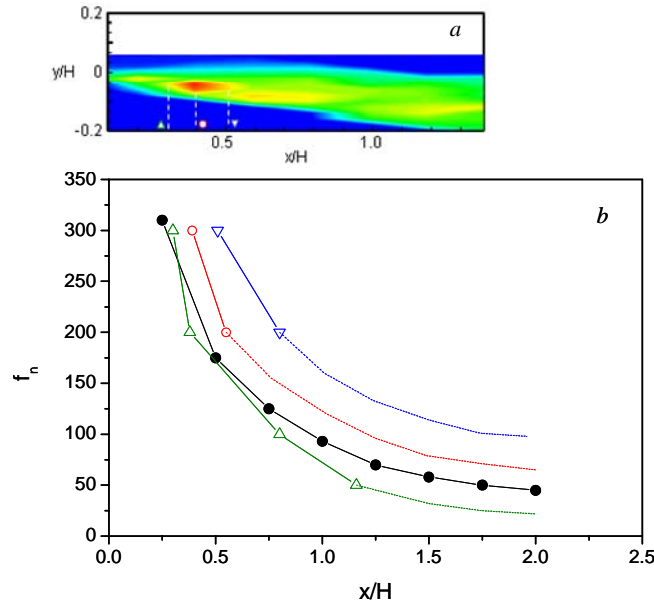


**Figure 5.** Raster plot of spectral energy at  $f = 300$  Hz in the baseline flow (a) and the plot of maximum spectral energy at discrete set of frequencies (b) at: peak ( $\circ$ ) and upstream ( $\triangle$ ) and downstream ( $\nabla$ ) boundaries. Also, results of the local stability analysis of measured baseline velocity profiles are shown ( $\bullet$ ). Contour levels:  $1E-4$  to  $5E-3$ .

## Actuated Flow

Direct, small-scale control of shear layer is effected via a periodic train of high-frequency vortex pairs that are injected into the baseline cross-flow through a spanwise array of actuators. To assess the dynamics of the vortex train interaction with the baseline flow, highly-resolved PIV measurements are taken within  $-0.2 < x/H < 0.8$  at different jet momentum coefficients  $C_\mu$ . The measurements are taken phase-locked to the actuation signal and raster maps of the calculated vorticity component are shown in Fig. 6 for three jet momentum coefficients. At a low level momentum coefficient ( $C_\mu = 0.004$ , Fig. 6a), the interaction of the actuator jets with the cross-flow is primarily confined to the wall boundary layer. The vorticity within the boundary layer is clearly temporally and spatially

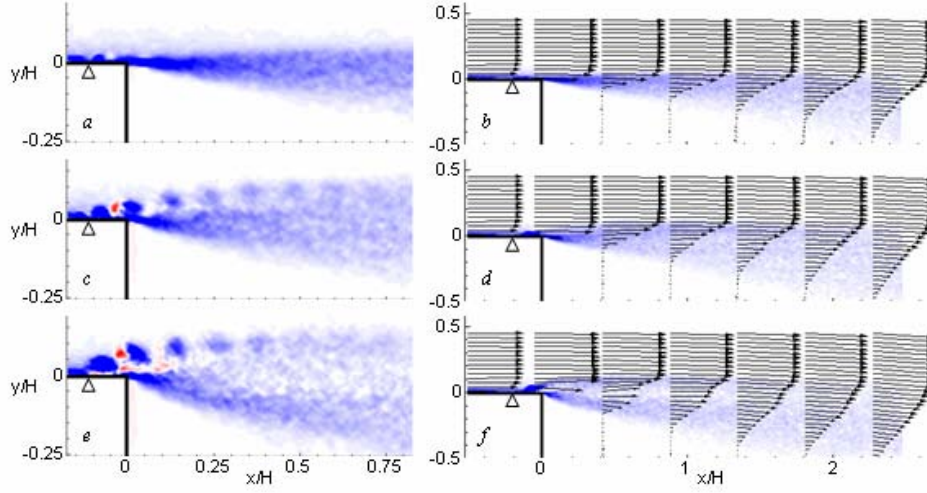


**Figure 6. Phase-averaged (a, c, e) and ensemble-averaged (b, d, f) vorticity field  $\zeta_x$  with overlaid mean vector profiles for the flow actuated at  $St = 7.36$  and  $C_\mu = 0.004$  (a, b),  $0.026$  (c, d), and  $0.051$  (e, f). Location of the actuator orifice is marked by a triangle. Vorticity  $\zeta_x$  ( $s^{-1}$ ) contour levels: -2500 ■ ■ 2500.**

modulated, with a weak counter clockwise (CCW) vortex preceding a dominant clockwise (CW) vortex. However, coherence of the CW vorticity rapidly diminishes within the shear layer. As the momentum coefficient of actuation increases, the jet vortices (which then have higher circulation) begin to protrude through the edge of the boundary layer and thereafter maintain their coherence farther downstream within the shear layer, primarily along its high-speed edge ( $C_\mu = 0.026$ , Fig. 6c). At the same time, stronger CCW vorticity concentrations become visible farther downstream, but are rapidly dissipated over a distance of 1.5 actuation wavelengths. It is clear that high-frequency actuation imposes a train of CW vortices that interact with the shear layer. Further increase in the jet momentum ( $C_\mu = 0.051$ , Fig. 6e) leads to an upstream separation of the jet vortices off the step surface and as a result the train of vortices separates from the high-speed edge of the shear layer. Nonetheless, the jet vortices still interact with the shear layer and begin to lose their coherence by  $x/H \sim 0.5$  as they are convected downstream. It is also noteworthy that the increase in the jet's momentum coefficient induces significant alteration in the overall structure of the shear layer which spreads substantially more towards the low speed side ostensibly owing to the vectoring by jet vortices near the step edge (e.g., compare Figs. 6a and e). This spreading of the layer is accompanied by a reduction in the magnitude of the vorticity in the upper region of the shear layer and induced upward flow along the vertical wall of the step. Accompanying the phase-averaged plots, the composite cross stream vorticity plots of the entire measurement domain  $-0.5 < x/H < 2.5$  are shown in Figs. 6b, d, and f, along with overlaid velocity profiles at equally-spaced downstream locations. The corresponding map for the unforced flow is shown in Fig. 3a. For actuation at  $C_\mu = 0.004$  (Fig. 6b), there is not much visible difference between the time-averaged velocity and vorticity fields of the unforced and forced flows (the vorticity magnitude decreases only slightly in the forced flow). As the momentum coefficient is increased (Fig. 6d,  $C_\mu = 0.026$ ), the shear layer spreads more towards the low speed side, the magnitude of the vorticity within the shear layer decreases, and there is a broadened vorticity concentration just upstream from the step edge. Ultimately, the jet is separated from the initial shear layer (Fig. 6f), but it is apparent that they merge in the downstream direction. Therefore, the varying jet momentum coefficient determines whether the main interaction between the high-frequency vortex train (of the jet) and shear layer will take place right from the shear layer formation (low  $C_\mu$ ), or be pushed further downstream, with the increasing  $C_\mu$ .

The effects of the actuation on the development of the shear layer are further characterized by its downstream evolution of the momentum thickness  $\theta$ , as shown in Fig. 7, along with the baseline case. At the lowest actuation level ( $C_\mu = 0.004$ ), there is no significant change in development of  $\theta$  relative to the baseline case, besides initial small increase that is followed by a small decrease in  $\theta$ . Contrary to this case, the other two actuations show a notable increase in spreading of the shear layer and the corresponding momentum thickness. It should also be noted

that the prominent growth of the shear layer occurs immediately downstream of the step edge (up to  $x/\theta_0 \approx 150$ ) and that the growth rates ( $d\theta/dx$ ) approach that of the baseline flow afterwards.

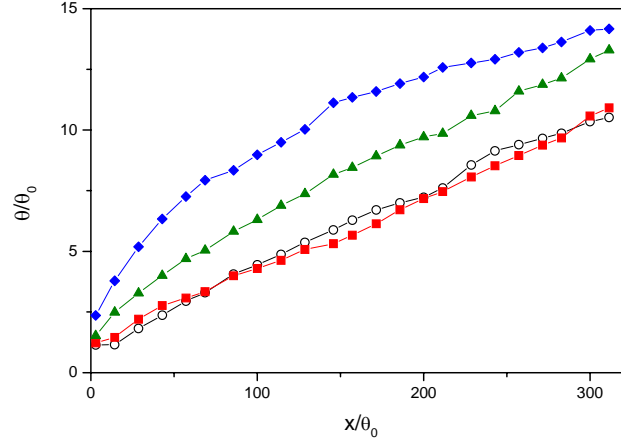


**Figure 7.** Evolution of the shear layer momentum thickness for the baseline ( $\circ$ ) and the flow actuated at  $St = 7.36$  and  $C_\mu = 0.004$  ( $\blacksquare$ ),  $0.026$  ( $\blacktriangle$ ), and  $0.051$  ( $\blacklozenge$ ).

One of the important consequences of the controlled flow field from the standpoint of its inviscid instability and the ensuing vortical motions is its altered mean flow structure. Fig. 8a compares the computed natural frequencies (of the most amplified perturbation according to Eq. (3)) for the free shear flow and the excited flow with high-frequency perturbations and  $C_\mu = 0.026$ . It can be seen that the natural frequency for both cases decreases with the distance from the step. Also, the upstream excitation causes a significant decrease of the natural frequency up to  $x/H=1.5$  or  $x/\theta_0 \approx 220$ . Therefore, the excited mean flow in this range of distance from the step is more stable to higher frequencies. Note, however, that the effect of upstream excitation decays with distance and beyond  $x/H=2$  ( $x/\theta_0 \approx 290$ ) the effect is minimal. The local linear stability analysis implies that the flow becomes more stable in the near field, as fundamental frequencies are lowered, and therefore, their formation lengths are extended in the downstream direction. Moreover, experimental measurements of the spectral energy at any specific energy-bearing,

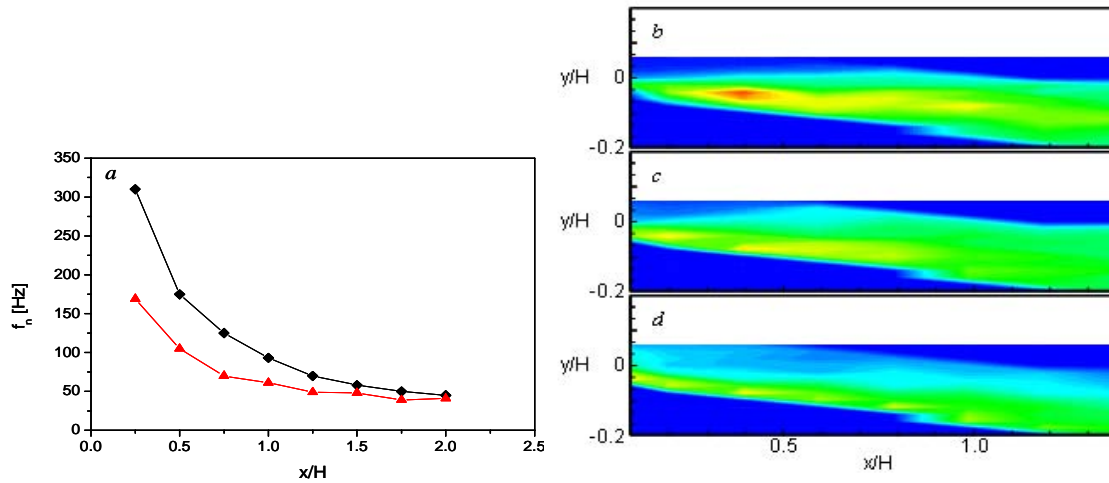


**Figure 8.** a) Calculated natural frequencies along the shear layer for the baseline ( $\blacklozenge$ ) and  $C_\mu = 0.026$  ( $\blacktriangle$ ). b) Raster plot of spectral energy at  $f = 300$  Hz in the flow actuated at  $St = 7.36$  and  $C_\mu = 0.004$  (b),  $0.026$  (c), and  $0.051$  (d). Contour levels are the same as in Fig. 5.

low frequency motion show reduction in energy of those scales under the controlled flow conditions. As an example, similar to the baseline case shown in Fig. 5a, the contour plots of the extracted energy content at frequency  $f = 300$  Hz from the spectral measurements are shown in Figs. 8b-d, for the actuated flows with  $C_\mu = 0.004, 0.026$  and  $0.051$ . When compared to the baseline spectral map (Fig. 5a), it is seen that the energy level of motions at  $f = 300$  Hz becomes progressively suppressed with the increase in  $C_\mu$ . In the case of motions at  $f = 300$  Hz, the peak energy reduction is in excess of 20% relative to the unforced flow.

Further spectral analysis of the velocity fluctuations in the baseline flow and controlled flows is focused on assessing how the energy content of different flow scales (frequencies) changes upon the application of open-loop control. Each controlled case is compared against the baseline flow with particular emphasis on the range of frequencies with either enhanced or suppressed energy after the control is applied. The crossover frequency that separates suppressed from enhanced frequencies in the flow is denoted as  $f_c$ . To illustrate several representative outcomes of such individual comparisons, Figure 9 shows an example of power spectra measured for the baseline flow and the flow actuated at  $St = 7.36$  and  $C_\mu = 0.026$  at  $x/H = 0.1$  ( $x/\theta_0 \approx 15$ ). Two mean streamwise velocity profiles are shown in Fig. 9a with three characteristic cross stream locations marked at  $y/H = -0.06, 0$ , and  $0.06$ , representing the low-speed edge, centre, and high-speed edge of the shear layer. It is noteworthy that the power spectra of the baseline shear layer does not contain discrete spectral components that indicate the rollup frequency of spanwise coherent vortical structures, which in part can be attributed to the deliberate tripping of the upstream boundary layer. As seen in Figs. 9b and c, significant energy content in baseline flow carry the scales up to the corresponding frequencies of  $f/f_d = 0.2$ , while the overall energy content along the high-speed edge is at least an order of magnitude lower, which indicates that zones of high fluctuating velocity components are tied to the central and low-speed domain of the shear layer. Between the central and low-speed edge regions, it is also indicative that energy content of small-scale (high-frequency) motions drops sharply along the low-speed edge, while there is a wide range of small-scale motions evolved within the shear layer centre. The resulting difference in power spectra of the controlled flow relative to the baseline clearly depends on the spatial domain. Two common features of all controlled power spectra are the appearance of focused peaks at actuation frequency  $f/f_d = 1$  and increase in energy content of the small scales. The peak at the actuation frequency is the strongest along the high-speed edge as these actuation vortices are carried into the shear layer along that path. Although both the low-speed (Fig. 9b) and high-speed (Fig. 9d) edge results yield an increase in overall energy across all scales (frequencies), there are different mechanisms behind this outcome. A strong increase in energy along the high-speed edge is caused by both the influx of small-scale motions via vortical train (Fig. 6c) and increased turbulent energy production (Fig. 13b). Large-scale energy content along the low-speed edge becomes enhanced during the active control due to the increased shear layer spreading and engulfing of nearly-stagnant fluid from below. The small-scale energy content becomes also enhanced as turbulent energy production increases and overall energy feed to the small scales is accelerated.

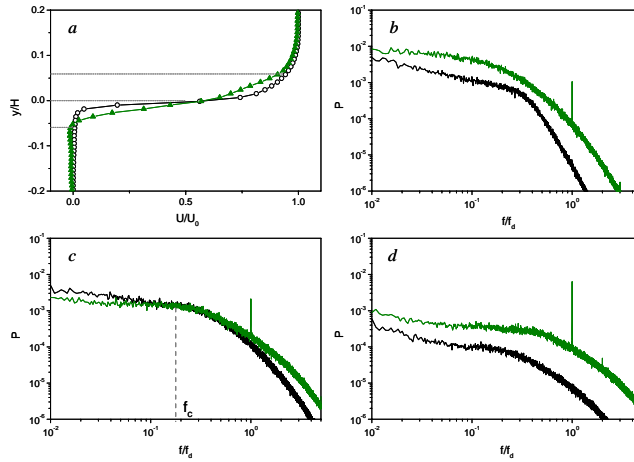


**Figure 9.** Mean streamwise velocity profiles (a) for the baseline (○) and the flow actuated at  $St = 7.36$  and  $C_\mu = 0.026$  (▲) at  $x/H = 0.1$  and the corresponding power spectra of velocity fluctuations at  $y/H = -0.06$  (b),  $0$  (c), and  $0.06$  (d).

The most intriguing energy redistribution in the controlled flow takes place in the shear layer central region, see Fig. 9c. The power spectrum of the forced flow exhibits strong peak at the actuation frequency and have two other notable features. First, even though the actuation is applied at  $f/f_d = 1$ , there is significant increase in energy content over a broad range of small scales (for  $f > f_c$ ). Second, simultaneously with the increased energy content of small scales, there is a decrease in energy at the large scales (low frequencies). Although the measuring point is in the region where the net effect of the actuation induces local increase in the turbulent kinetic energy (Fig. 13a), these results show that energy content of the large scales actually decreases while energy of the small scales increases. Therefore, it is argued that actuation actually affects the energy balance between the two ends of the spectrum and enhances energy transfer to small scales, with an ultimate further transfer of energy into dissipation.

Complete spectral results are shown in Fig. 10 as contour plots of the crossover frequency  $f_c$ , which delineates the frequencies up to which the energy content of the large scales is lowered as a consequence of the dissipative actuation and above which the energy of the small scales is enhanced (relative to the baseline flow). Three-color palette for the contour plots is set such that neutral (white) matches  $f_c/f_d = 1$ , i.e., it marks scenario in which the frequencies below the actuation frequency  $f_d$  are suppressed, while the frequencies above  $f_d$  have enhanced energy due to the active flow control. As  $f_c$  moves to the lower frequencies ( $f_c < f_d$ ), its contour becomes darker blue in color. Opposite, as  $f_c$  moves to the higher frequencies ( $f_c > f_d$ ), its contour becomes darker red in color. Therefore, the low limit scenario when all scales have energy lowered in the controlled flow relative to the baseline is represented as the darkest blue color, while the upper limit, when all scales in the controlled flow have their energy enhanced, is represented by the darkest red color. The present spectral results for  $C_\mu = 0.004$  are shown in Fig. 10a. It is seen that initial suppression of energy across the large scales spreads almost uniformly across the shear layer and that a range of affected scales rapidly increases toward the small scales. In other words, an initial narrow-band increase in energy of the small scales is rapidly dissipated with downstream distance and the energy over all scales is already suppressed downstream of  $x/H = 0.2 - 0.3$  (or  $x/\theta_0 \approx 30 - 45$ ). Therefore, the effect of the dissipative control can be viewed as having a stabilizing impact in terms of the overall suppression of the fluctuations across all scales. The contour plots of  $f_c$  in Figure 10b-c suggest that the transfer of energy among the scales is significantly altered with the increase in  $C_\mu$ . Already at  $C_\mu = 0.026$  (Fig. 10b), an initial sharp increase of the range of scales with lower energy is visible in the centre of the shear layer but both the high- and low-speed edges show overall increase in spectral energy across wide range of scales. The high-speed edge of increased energy (zone A) is induced by the influx of the high-frequency vortices and increased turbulent energy production. It is also seen that this zone of

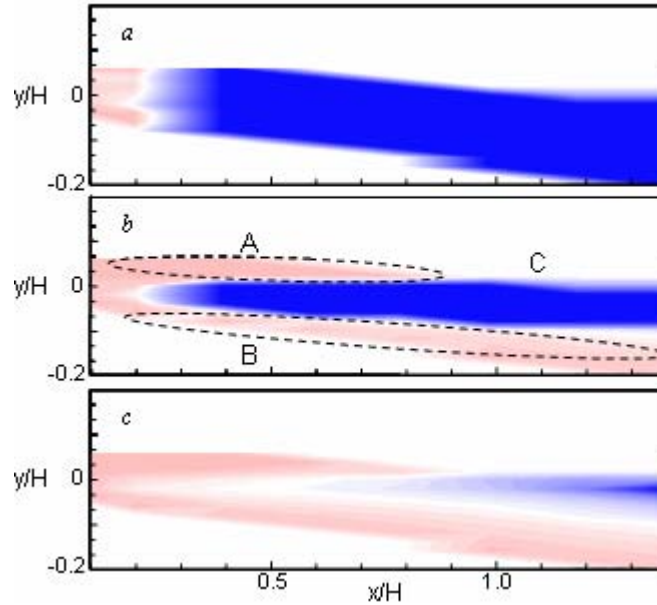


**Figure 10.** Contour plots of the crossover frequency  $f_c$  for the flow actuated at  $St = 7.36$  and  $C_\mu = 0.004$  (a), 0.026 (b), and 0.051 (c).



increased energy narrows in the downstream direction as the high-frequency vortices lose their coherence and turbulent production weakens. Along the low-speed edge (zone B), spectral energy increases due to the shear layer enhanced spreading under active control, and initially due to the increased turbulent energy production. As the energy in this region is mostly fed through the large-scale motion of the engulfed fluid, the actuation effect is long lasting and reduction in energy over wide-band scales is not detected in the measurement domain. The strongest decrease in energy occurs within the centre of the shear layer (zone C) and spreads slowly in the downstream direction over its boundaries. As  $C_\mu$  is increased to the highest level (Fig. 10c), all three characteristic zones denoted in Fig. 10b are pushed further downstream. As the vortex train protrudes further into the flow and vectors the shear layer more towards the low-speed side (Fig. 6e), zones of increased spectral energy initially spread over a longer downstream distance, disabling the transition to the suppression of spectral energy in the shear layer centre. Therefore, only the beginning of the zone C is registered within the measurement domain in Fig. 10c.

Nonlinear PSE analysis (using Eq. (5)) of the baseline computed backward facing step flow at  $Re=43,000$  gives insight into the nonlinear complex interaction between the various modes of perturbations along the shear layer. Six modes at the specific frequencies  $\omega = m$  where  $m = 1, 2, 3, 4, 5, 6$  are considered. The local linear spatial stability analysis at  $x=0$  provides the upstream conditions for the perturbations' normalized shape functions. Initial amplitudes are:  $\varepsilon_{10}=10^{-5}$ ,  $\varepsilon_{20}=10^{-5}$ ,  $\varepsilon_{30}=10^{-6}$ ,  $\varepsilon_{40}=10^{-6}$ ,  $\varepsilon_{50}=10^{-7}$ ,  $\varepsilon_{60}=10^{-7}$  with  $\varepsilon_{-m0} = \varepsilon_{m0}$ . These values may mimic regularly ordered, small turbulent perturbations entering the shear layer or a shear layer excited by upstream low-frequency perturbations (at frequencies of 44 Hz and 88 Hz in the experiments). The resulting field of stream function perturbation (Fig. 11a) shows that the low-frequency modes grow along the shear layer. The  $\omega = 2$  (88 Hz) mode dominates the perturbations in the range  $1 \leq x/H \leq 2$ . This is in agreement with Fig. 5b which shows a dominant frequency between 50 Hz and 100 Hz in this range. To demonstrate the effect of a high-frequency upstream excitation, the initial amplitude of the sixth mode (with  $\omega = 6$ ) is now increased to  $10^{-5}$  while all other amplitudes are kept the same as above. Here the amplitude of mode 6 is same as that of modes 1 and 2. This may mimic a case of excitation at 265 Hz (or  $St = 0.98$ ) in the experiment. The resulting stream function field for this case is shown in Fig. 11b. It can be seen that a high-frequency perturbation dominates the shear layer within a distance of up to  $x/H = 1.5$  or  $x/\theta_0 \approx 220$  from the step. In this range of influence low-frequency perturbations are not dominant. However, downstream of this distance low-frequency perturbations reappear and dominate the flow exactly as in previous case. This behaviour is similar to that in Fig. 6, although actuation frequency is not as high as in the experiments. Note that with the grid of baseline flow used and existing computational power, the NPSE analysis can not resolve modes with frequencies greater than  $\omega = 7$ .

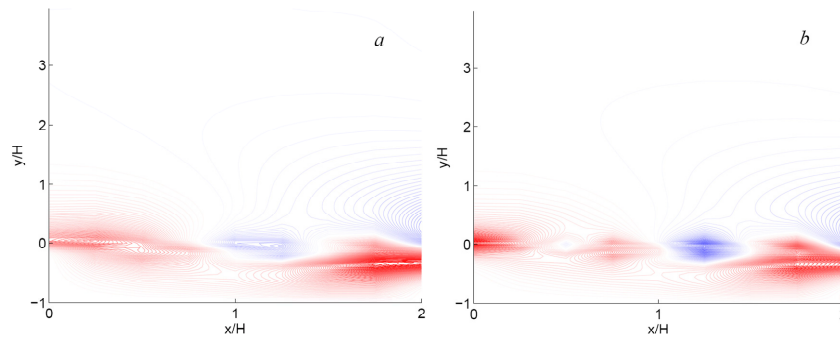


**Figure 11. NPSE-computed field of stream function perturbation along the shear layer for the case of low- (a) and high- (b) frequency actuation.**

Further analysis assesses how dissipative, high-frequency actuation affects distribution of turbulent kinetic energy (TKE), which is estimated as  $k = (\overline{u'^2} + \overline{v'^2})/2$ . Measured TKE profiles are plotted in Figs. 12a-c for the baseline flow and the flows controlled at  $St = 7.36$  and  $C_\mu = 0.004, 0.026$ , and  $0.051$ . At locations closest to the step edge ( $x/H = 0.1$ , Fig. 12a), the baseline flow exhibits a highly focused profile of TKE within a narrow shear layer. Controlled

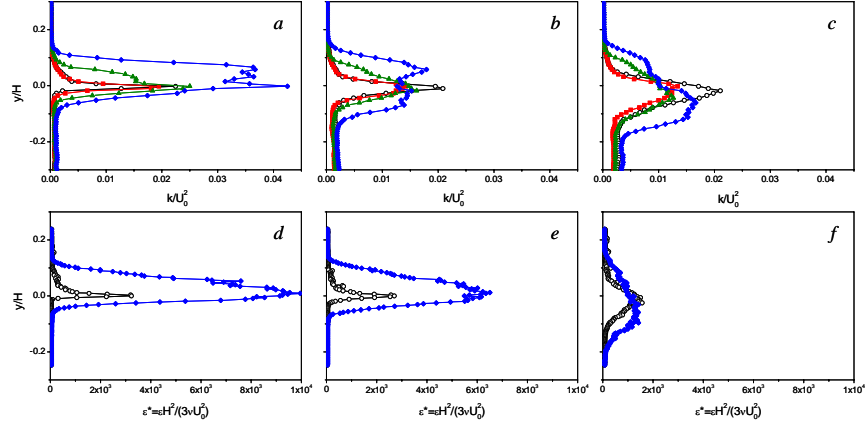


**Figure 12. Profiles of TKE  $k^*$  at  $x/H = 0.1$  (a),  $0.25$  (b),  $0.5$  (c), and TKE dissipation rate  $e^*$  at  $x/H = 0.05$  (d),  $0.1$  (e), and  $0.5$  (f), for the baseline ( $\circ$ ) and the flow actuated at  $St = 7.36$  and  $C_\mu = 0.004$  ( $\blacksquare$ ),  $0.026$  ( $\blacktriangle$ ), and  $0.051$  ( $\blacklozenge$ ).**

flow at the lowest  $C_\mu$  has weakly altered TKE profile showing a slight increase in spreading to the low-speed side, but with reduction in peak TKE to  $k/U_0^2 = 0.02$  from  $0.024$  of the baseline flow. As  $C_\mu$  is increased to  $0.026$ , the shear layer spreading on the low-speed edge becomes more prominent, with the peak TKE exceeding the baseline case. There is also a significant increase in the TKE level over the high-speed edge due to direct jet penetration further downstream and the consequent addition of convected TKE by the jets. The “break” between the jet and the shear layer becomes even more pronounced for the highest  $C_\mu$  case, and is marked by the presence of two distinct peaks in the profile. The peak on the high-speed edge corresponds to the convected high levels of TKE by the high-frequency jets, whose penetration length further increases with the increase in  $C_\mu$ . Such a double-peak is also visible in the corresponding vorticity plots (Fig. 6f). The addition of TKE energy along the high-speed edge clearly enhances energy levels within the shear layer, as the peak TKE becomes almost twice the corresponding baseline peak. As a further consequence of increased TKE levels, the flow continues to spread more towards the low-speed edge and the shear layer broadens. By the next downstream location ( $x/H = 0.25$ , Fig. 12b), the peak of the low-speed side of the flow is significantly broader, a significant addition of TKE by the convected jets is largely dissipated even for the highest  $C_\mu$  case. Note that simultaneously with the shear layer broadening with increase in  $C_\mu$ , peak TKE becomes significantly suppressed in any of the controlled cases, when compared to the baseline flow. At the last downstream position shown ( $x/H = 0.5$ , Fig. 12c), already noted trend continues: the direct contribution in TKE energy by the jets weakens along the high-speed edge, while the shear layer spreading over the low-speed edge increases with  $C_\mu$ , as more low-speed fluid gets engulfed into the shear layer. Again, it should be noted that peak shear layer TKE levels are significantly suppressed in the controlled flows. The other notable feature is that the TKE levels become suppressed across the shear layer for the lowest  $C_\mu$  case, if compared to the baseline flow. Another indication of the shear layer “vectoring” towards the low-speed side is the migration of the peak TKE with the increase in  $C_\mu$ . The effect of high-frequency forcing on turbulent dissipation rate  $\varepsilon$  is also quantified, and dissipation profiles are shown in Figs. 12d-f at three downstream locations  $x/H=0.05$ ,  $0.1$ , and  $0.5$ . At the nearest location to the step edge (Fig. 12d), there is the strongest increase in the spatial domain with enhanced dissipation, as well as the strongest increase in  $\varepsilon$  absolute magnitude. It should be noted that the dissipation increase is more pronounced at the high-speed side of the shear layer than on the low-speed side, as a direct consequence of the convection of the high-frequency vortices into the shear layer. As the flow evolves in the downstream direction, there are several trends that can be noted: (i) absolute magnitude of  $\varepsilon$  decreases and eventually approaches the magnitude in the baseline flow, (ii) spreading of the zone with increased dissipation becomes more pronounced along the low-speed side while initial strong increase along the high-speed side subsides, and (iii) the peak  $\varepsilon$  magnitude becomes displaced towards the low-speed side. Overall, it is believed that closely coupled localized strong enhancement in both turbulent energy production and dissipation rate prematurely drain energy from the mean flow upon actuation (relative to uncontrolled flow) and contributes to its stabilization later on. Such domain

of the localized stabilization is spatially-dependent on the momentum coefficient of high-frequency actuation, and can develop closer to the shear layer origin for the low  $C_\mu$ , or be pushed further downstream for higher  $C_\mu$ .

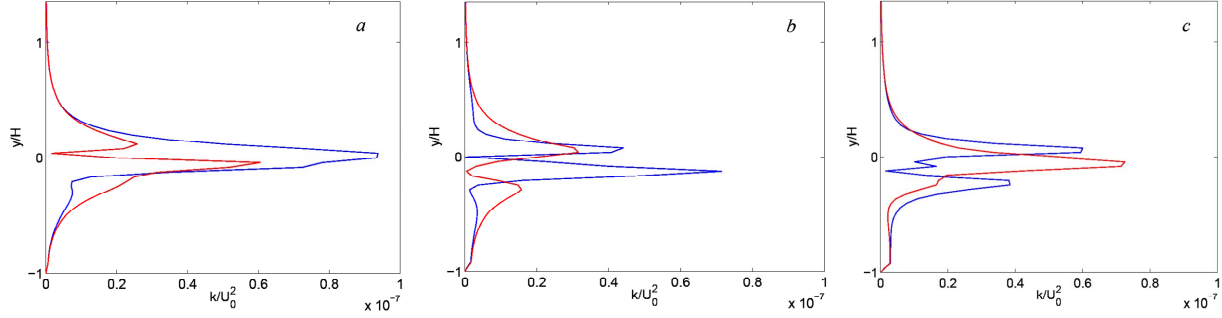


**Figure 13.** Profiles of TKE at  $x/H = 0.25$  (a),  $0.5$  (b),  $0.75$  (c) and the flow actuated at  $St=0.96$  and  $\epsilon_06=10^{-7}$  (red line) and  $10^{-5}$  (blue line).

The effect of high-frequency actuation on the distribution of TKE along the shear layer is also assessed from the NPSE computations (Figs. 13a-c). Although perturbations are much smaller than in the experiments (a limitation of the PSE formulation for relatively short shear layers as in the present case), similar trends to those in Figs. 12a-c are observed. At locations closest to the step edge ( $x/H = 0.25$ , Fig. 13a), the flow with regularly ordered, small upstream perturbations exhibits a focused TKE profile within a narrow shear layer that decreases in its peak and becomes wider at ( $x/H = 0.5$ , Fig. 13b) and then peaks again at ( $x/H = 0.75$ , Fig. 13c). Increasing the amplitude of the higher frequency mode 6 ( $St = 0.98$ ) has altered TKE profile showing an increase in spreading to the shear layer low-speed side at  $x/H = 0.5$  (Fig. 13b), but with reduction in peak TKE. At  $x/H = 0.75$  (Fig. 13c) the effect of the higher frequency excitation decays and at downstream locations low frequency perturbations dominate the flow again.

Distributions of integrated turbulent kinetic energy across the shear layers are shown in Fig. 14a for the baseline, and three controlled flows ( $C_\mu = 0.004$ ,  $0.026$ , and  $0.051$ ). It is expected that the total energy across the shear layer initially increases in part due to the influx of energy carried by the high-frequency vortices. Indeed, all three controlled cases show initial increase in  $k$ , directly proportional to  $C_\mu$ . The highest  $C_\mu$  clearly induces the highest increase in total energy, but as the control effect diminishes downstream,  $k$  starts to approach the baseline case from above. After a short initial increase in  $k$  up to  $x/H \approx 0.5$  ( $x/\theta_0 \approx 73$ ), middle  $C_\mu$  generates total TKE comparable to the baseline case in the remaining measurement domain, while it is indicative that the lowest  $C_\mu$  control leads toward suppressed total TKE throughout the measurement domain after  $x/H \approx 0.1$  ( $x/\theta_0 \approx 15$ ). Significant initial increase in total kinetic energy is partially attributed to the influx of energy carried by the small-scale control vortices, but as they also interact with the shear layer and lose its coherence, it is expected that the production rate of TKE becomes

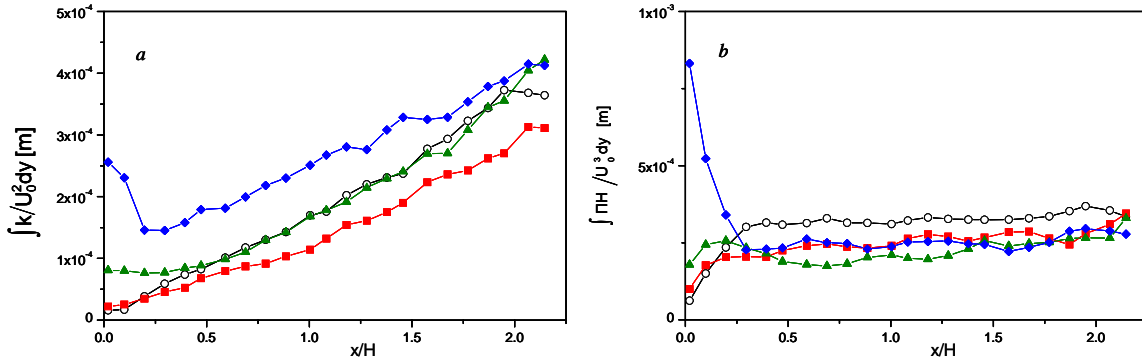


**Figure 14.** Evolution of the cross-stream integrated (a) and averaged (b) TKE  $k$  for the baseline ( $\circ$ ) and the flow actuated at  $St = 7.36$  and  $C_\mu = 0.004$  ( $\blacksquare$ ),  $0.026$  ( $\blacktriangle$ ), and  $0.051$  ( $\blacklozenge$ ).



thereby enhanced. To assess the effect of dissipative control on production of TKE in the shear layer, integrated turbulent energy production ( $\Pi$ ) across the shear layer is calculated and shown in Fig. 14b. As seen in Fig. 14b, integrated  $\Pi$  steadily increases in the baseline flow up to  $x/H = 0.4$  and thereafter remains relatively flat. The control at  $C_\mu = 0.004$  induces a weak and short initial increase in  $\Pi$ , which is followed by a significant suppression of overall production throughout the measurement domain. At  $C_\mu = 0.026$ , there is a more pronounced and slightly longer initial domain of increased  $\Pi$ , which is again followed by a large domain of pronounced suppression of production. Finally, in spite of a large initial increase in  $\Pi$  for the highest  $C_\mu$  case, the shear layer generates less turbulent motions starting as close as  $x/H = 0.3$  ( $x/\theta_0 \approx 50$ ).

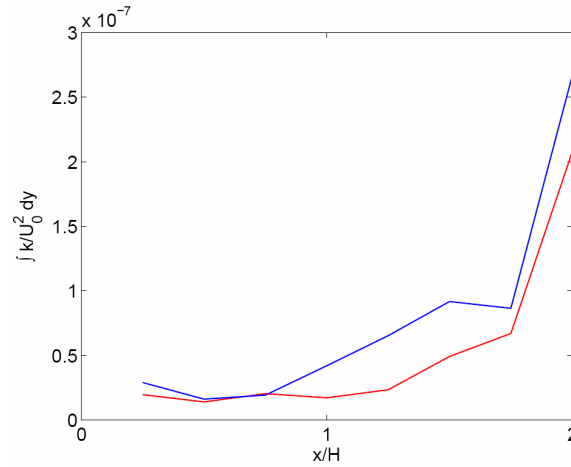


**Figure 15. Evolution of the cross-stream integrated (a) TKE  $k$  for the flow actuated at  $St = 0.96$  and  $\epsilon_{06} = 10^{-7}$  (red line) and  $10^{-5}$  (blue line).**

The integrated perturbations kinetic energy across the shear layer are also computed from the NPSE analysis (Fig. 15). Again, although perturbations are much smaller than in the experiments, the trends are similar to the experimental results in Fig. 14a. The flow with regularly ordered, small upstream perturbations shows a gradual growth of the integrated TKE long the layer. The flow with the increased amplitude of the higher frequency mode 6 shows a decrease in the integrated TKE with minimum at  $x/H \sim 0.5$  and levels comparable to the previous case. At  $x/H > 0.7$  the integrated TKE of the controlled case increases again and at  $x/H > 1.5$  levels are similar to those of the previous case.

## Conclusions

The effects of high-frequency fluidic actuation on the evolution of small- and large-scale motions in a turbulent shear layer downstream of a backward-facing step can be investigated experimentally and numerically. It is demonstrated that dissipative, high-frequency actuation on effect the shear layer evolution through three domains (see Fig. 1). For instance, analyzed cases yield approximate boundaries of Domain I,  $0 < x/H < 0.3$  or  $0 < x/\theta_0 < 45$ , where localized dissipative, small scales enhance the turbulent kinetic energy production and dissipation rate. Domain II,  $0.3 < x/H < 0.7$  or  $45 < x/\theta_0 < 100$ , where a stabilized shear layer exists, marked by concomitant suppression of turbulent kinetic energy production and dissipation rate. In domain III,  $x/H > 0.7$  or  $x/\theta_0 > 100$ , the inviscid instability reappears but at lower natural frequencies and larger scales than those in the free layer.

## Acknowledgement

This research is supported by The Boeing Company and the Airforce Research Laboratory at Wright-Patterson under the FLOWCAD program.

## References

- [1] M. Amitay, A.M. Honohan, M. Trautman, & A. Glezer. Modification of the Aerodynamic Characteristics of Bluff Bodies Using Fluidic Actuators. *AIAA Paper 97-2004*, 1997.
- [2] J. M. Wiltse & A. Glezer. Direct Excitation of Small Scale Motions in Free Shear Flows. *Physics of Fluids*, 8:2026-2036, 1998.
- [3] S. A. Davis & A. Glezer. The Manipulation of Large- and Small-Scales in Coaxial Jets using Synthetic Jet Actuators. *AIAA Paper 2000-0403*, 2000.
- [4] B. L. Smith & A. Glezer. The Formation and Evolution of Synthetic Jets. *Physics of Fluids*, 10:2281-2297, 1998.
- [5] A.M. Honohan, M. Amitay, & A. Glezer. Aerodynamic Control using Synthetic Jets. *AIAA Paper 2000-2401*, 2000.
- [6] A. Glezer, M. Amitay, & A.M. Honohan. Aspects of Low- and High-Frequency Aerodynamic Flow Control. *AIAA Paper 2003-533*, 2003.
- [7] A.B. Cain, M.M. Rogers, V. Kibens, & G. Raman. Simulations of High-Frequency Excitation of a Plane Wake. *AIAA Paper 2001-0514*, 2001.
- [8] F.S. Alvi, R. Elavarsan, C. Shih, G. Garg, & A. Krothapalli. Control of Supersonic Impinging Jet Flows using Microjets. *AIAA Journal*. 41(7):1347-1355, 2001.
- [9] M.J. Stanek, G. Raman, V. Kibens, J.A. Ross, J. Odedra, & J. Peto. Control of Cavity Resonance through very High Frequency Forcing. *AIAA Paper 2000-1905*, 2000.
- [10] W.W. Bower, V. Kibens, A.W. Cary, F.S. Alvi, G. Raman, A. Annaswamy, & N.M. Malmuth. High-Frequency Excitation Active Flow Control for High-Speed Weapon Release (HIFEX). *AIAA Paper 2004-2513*, 2004.
- [11] S. Arunajatesan, J.D. Shipman, & N. Sinha. Hybrid RANS-LES Simulation of Cavity Flow Fields with Control. *AIAA Paper 2002-1130*, 2002.
- [12] L.L. Shaw, B.R. Smith, & S. Saddoughi. Full-Scale Flight Demonstration of Active Control of a Pod Wake. *AIAA Paper 2006-3185*, 2006.
- [13] D.P. Rizzeta & M.R. Visbal. Large-Eddy Simulation of Supersonic Cavity Flowfields Including Flow Control. *AIAA Journal*, 41:1452-1462, 2003.
- [14] M.J. Stanek, N. Sinha, J.M. Seiner, B. Pearce, & M.I. Jones. High Frequency Flow Control—Suppression of Aero-Optics in Tactical Directed Energy Beam Propagation and the Birth of a New Model (Part I). *AIAA Paper 2002-2272*, 2002.
- [15] M.J. Stanek, G. Raman, J.A. Ross, J. Odedra, J. Peto, F. Alvi, & V. Kibens. High Frequency Acoustic Suppression: The Role of Mass Flow, the Notion of Superposition, and the Role of Inviscid Instability – a New Model (Part II). *AIAA Paper 2002-2404*, 2002.
- [16] M. Gaster, E. Kit, & I. Wygnanski. Large-scale structure in a forced turbulent mixing layer. *J. Fluid Mechanics*, **150**, 23-38, 1985.
- [17] M.J. Day, N.N. Mansour, & W.C. Reynolds. Nonlinear stability and structure of compressible reacting mixing layers. *J. Fluid Mechanics*, **446**, 375 – 408, 2001.

# Experimental and Numerical Investigation of Controlled, Small-Scale Motions in a Turbulent Shear Layer

Bojan Vukasinovic, Ari Glezer

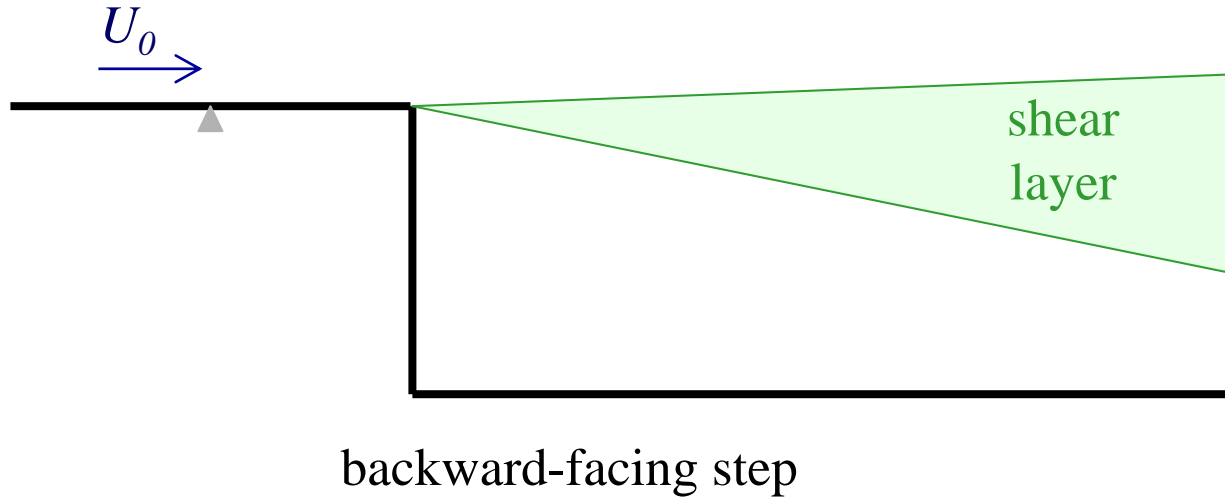
*Woodruff School of Mechanical Engineering  
Georgia Institute of Technology*

Zvi Rusak

*Department of Mechanical, Aerospace, and Nuclear Engineering  
Rensselaer Polytechnic Institute*

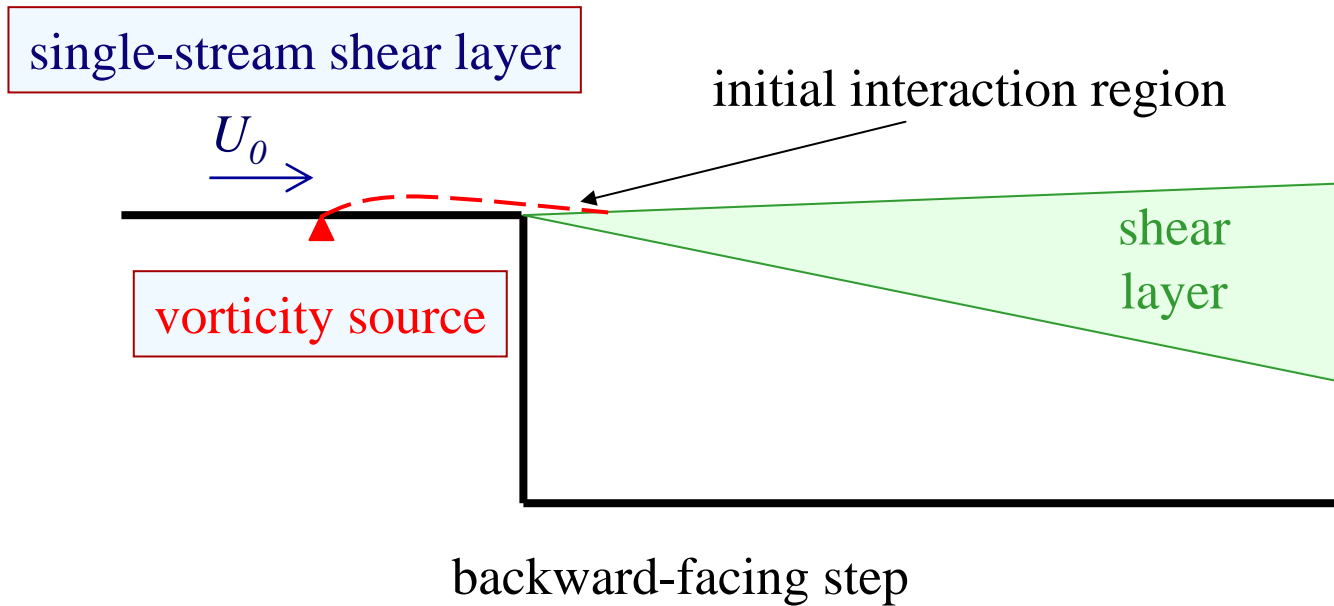
# Controlled Vorticity Manipulation

single-stream shear layer



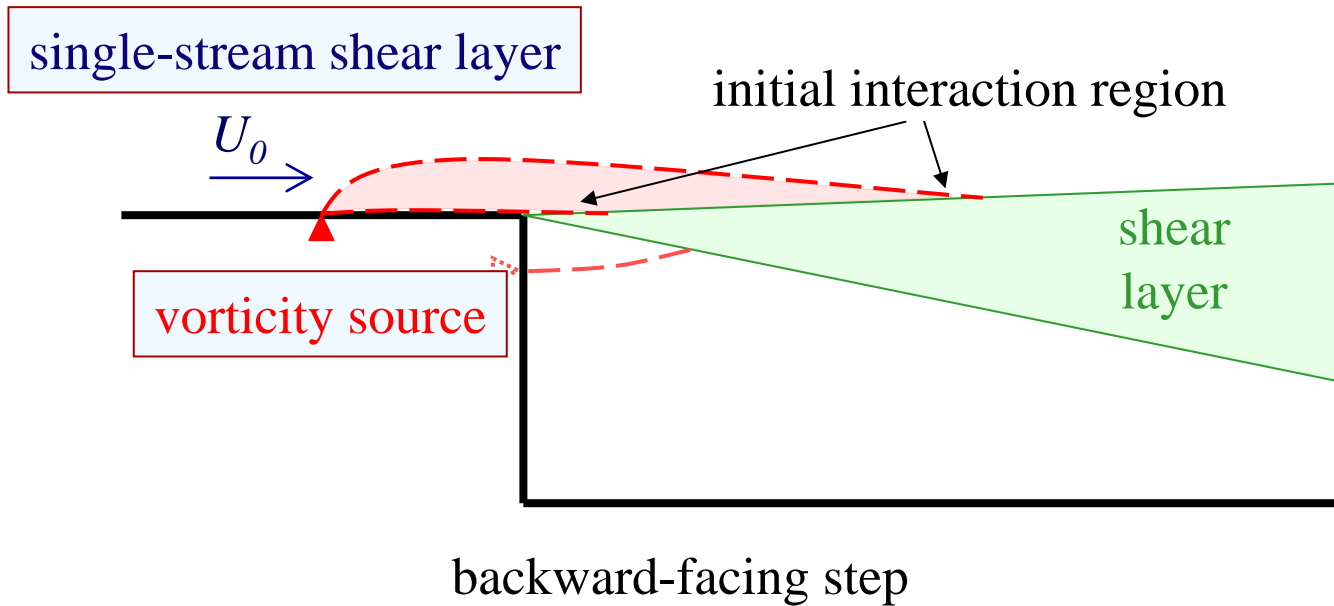
- Interaction with baseline flow through the free stream

# Controlled Vorticity Manipulation



- Interaction with baseline flow through the free stream
- Vorticity source (e.g., synthetic jet actuator)
  - » High-frequency vorticity ejection
  - » Actuation frequency can be varied

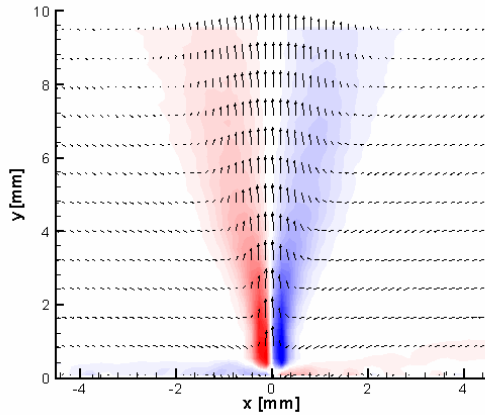
# Controlled Vorticity Manipulation



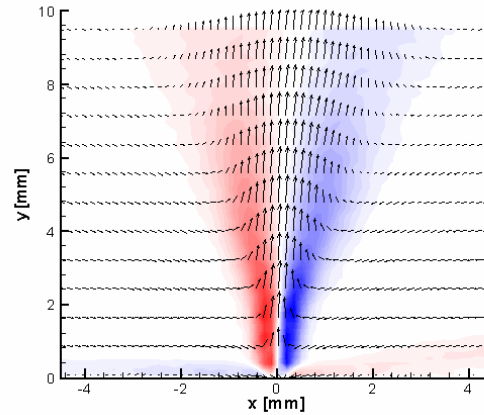
- Interaction with baseline flow through the free stream
- Vorticity source (e.g., synthetic jet actuator)
  - » High-frequency vorticity ejection
  - » Actuation frequency can be varied
  - » Vortex circulation is adjustable
  - » Wall shear stress and turbulent production are altered

# Vorticity Source

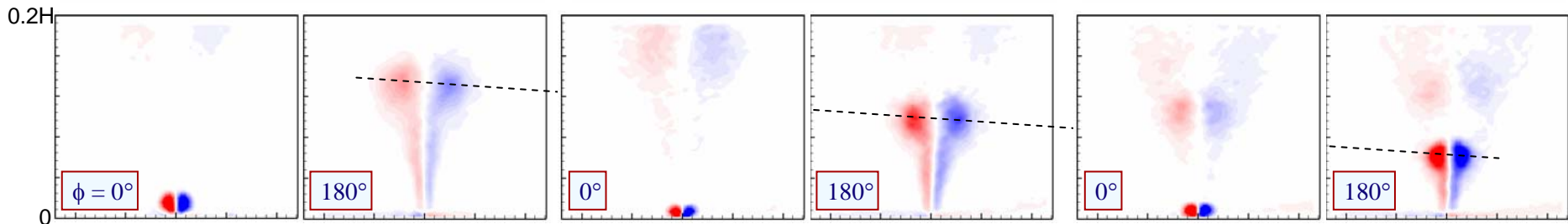
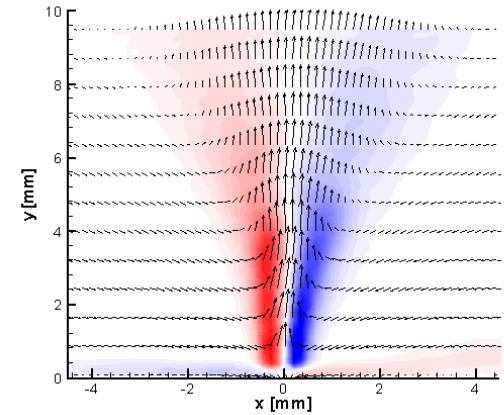
$f = 500 \text{ Hz } (U_j = 20 \text{ m/s})$



$f = 1000 \text{ Hz } (U_j = 30 \text{ m/s})$

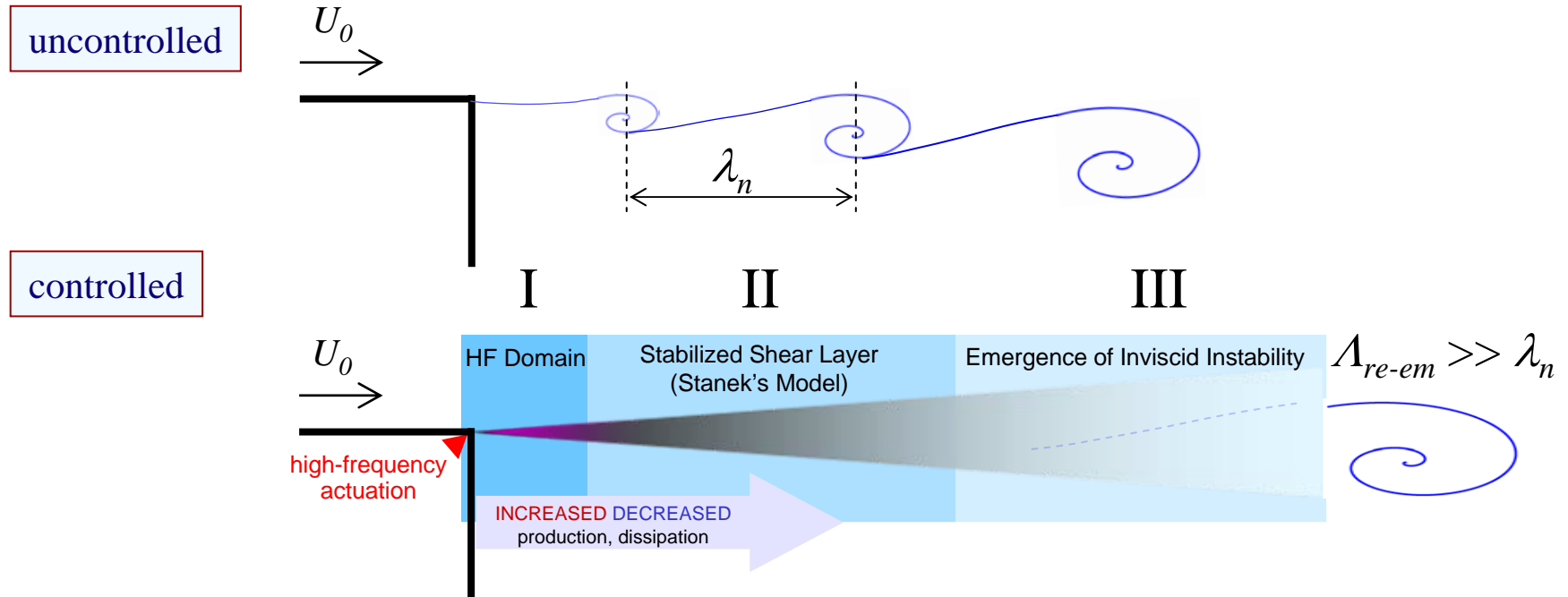


$f = 2000 \text{ Hz } (U_j = 30 \text{ m/s})$



- Control actuators generate synthetic jets into the cross flow
- Nominal jets issued at  $f = 2000 \text{ Hz}$  ( $St \sim 7$ )
- Jets can be synthesized from 2000 to 200 Hz with decreasing  $U_j$

# High-Frequency (Dissipative) Control

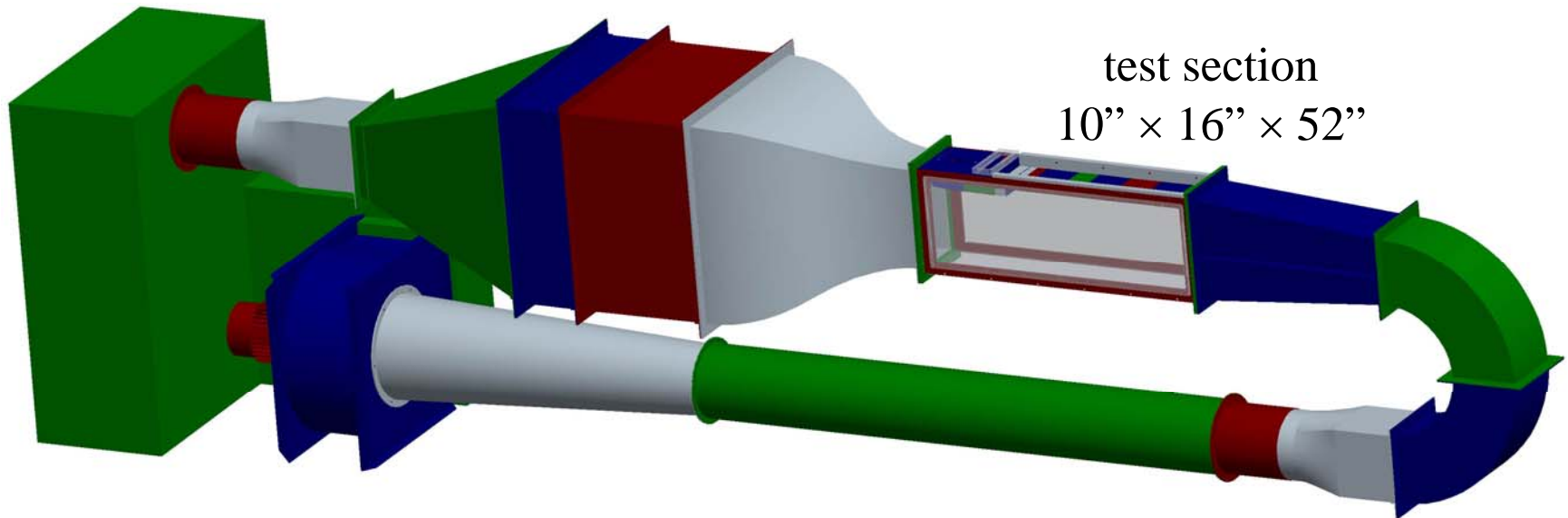


- **Region I: HF Actuation** increased dissipation and turbulent production leads to modification of the time-averaged baseline.
- **Region II: Stabilized Shear Layer** suppression of fundamental coherent vortices formation, reduced turbulent production and dissipation.
- **Region III: Re-emergence of Inviscid Instability** at a lower frequency.



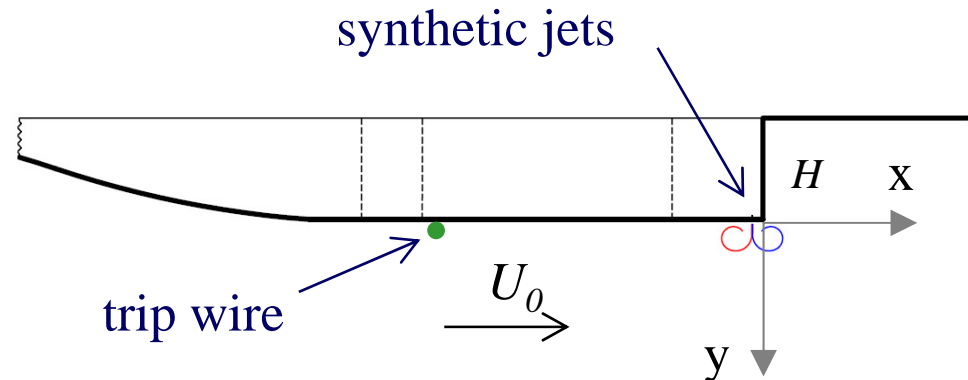
# Experimental Facility

- Closed-loop, low-speed wind tunnel; free stream turbulence intensity  $\sim 0.5\%$



## Flow-diagnostics

- Particle image velocimetry (PIV)
- Hot-wire anemometry (HWA)



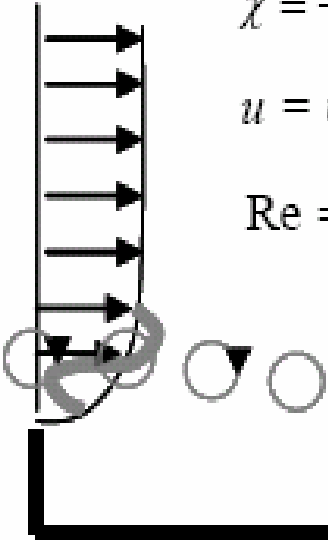
# Theoretical Tools I

- Mathematical Model

$$\psi = \psi_0(y) + \delta g(y, t)$$

$$U = U(y) + \delta g_y(y, t)$$

$$\chi = -U_y - \delta g_{yy}(y, t)$$

$$u = v = 0$$


$$\chi_t + \psi_y \chi_x - \psi_x \chi_y = \frac{1}{\text{Re}} (\chi_{xx} + \chi_{yy}),$$

$$\chi = -(\psi_{xx} + \psi_{yy}).$$

$$u = \psi_y, \quad v = -\psi_x$$

$$\text{Re} = \rho U H / \mu.$$

$$v = 0$$

$$\chi_x = 0$$

$$u = v = 0$$

- 2-D, unsteady, incompressible viscous flow
- Navier-Stokes equations in vorticity and stream function formulation

# Theoretical Tools II

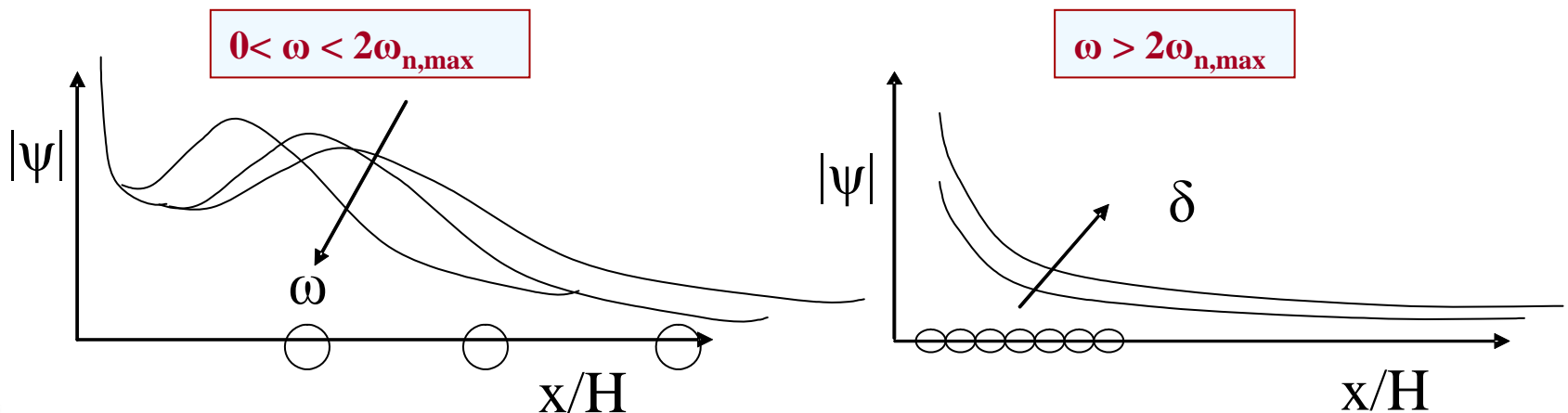
- Linear temporal and spatial stability studies; natural frequency  $\omega_n$  along base shear layer

$$\psi_1(x, y, t) = \phi(y) \exp[i(\alpha x - \omega t)]$$

$$L(\phi) = (U(x, y)\alpha - \omega)(\phi_{yy} - \alpha^2 \phi) - \alpha U_{yy}(x, y)\phi + \frac{i}{\text{Re}}(\phi_{yyy} - 2\alpha^2 \phi_{yy} + \alpha^4 \phi) = 0, \text{ as } |y| \rightarrow \infty, \phi \rightarrow 0.$$

- Second-order stability analysis; the flow linear frequency response;  $\tilde{x} = \varepsilon x$ ;  $\varepsilon = H/l_s$

$$\psi_1 = \underbrace{A(\tilde{x}, \omega) \exp \left[ \int_0^{\tilde{x}} \alpha_I(\tilde{x}', \omega) d\tilde{x}' \right]}_{\text{perturbation's amplitude}} \times \underbrace{\sqrt{\phi_R^2(\tilde{x}, y, \omega) + \phi_I^2(\tilde{x}, y, \omega)}}_{\text{shape function}} \times \underbrace{\sin \left[ \omega t - \int_0^{\tilde{x}} \alpha_I(\tilde{x}', \omega) d\tilde{x}' + \varphi(\tilde{x}, y, \omega) \right]}_{\text{periodic in time and space}}$$





# Theoretical Tools III

- Nonlinear parabolic stability equations (NPSE); nonlinear interaction between  $M+1$  modes

$$\psi_1(x, y, t) = \sum_{m=-M}^M \varepsilon_{m0} \phi_m(x, y) \exp \left[ \int_0^x a_m(x') dx' - im\omega_0 t \right]$$

- $2M+1$  parabolic equations

$$\begin{aligned} \varepsilon_{m0} \left\{ L_0(\phi_m, \tilde{\chi}_m) + L_1(\phi_{mx}, \tilde{\chi}_{mx}) + L_2(\phi_m, \tilde{\chi}_m) a_{mx} + L_3(\phi_{my}, \tilde{\chi}_{my}) \right\} = \\ \sum_{k=-M}^{M-1} \varepsilon_{k0} \varepsilon_{l0} \left[ a_k \phi_k (\tilde{\chi}_{ly} - 2a_l \phi_{ly}) + \phi_{kx} (\tilde{\chi}_{ly} + 2a_k^2 \phi_{ly}) - (\tilde{\chi}_{kx} + a_k \tilde{\chi}_k - a_k (a_{kx} - a_{lx}) \phi_k) \phi_{ly} \right] \\ \times \exp \left[ \int_0^x (a_k + a_l - a_m) dx' \right] \quad \text{where} \quad \tilde{\chi}_m = - (a_m^2 \phi_m + \phi_{myy}) \end{aligned}$$

**Linear**

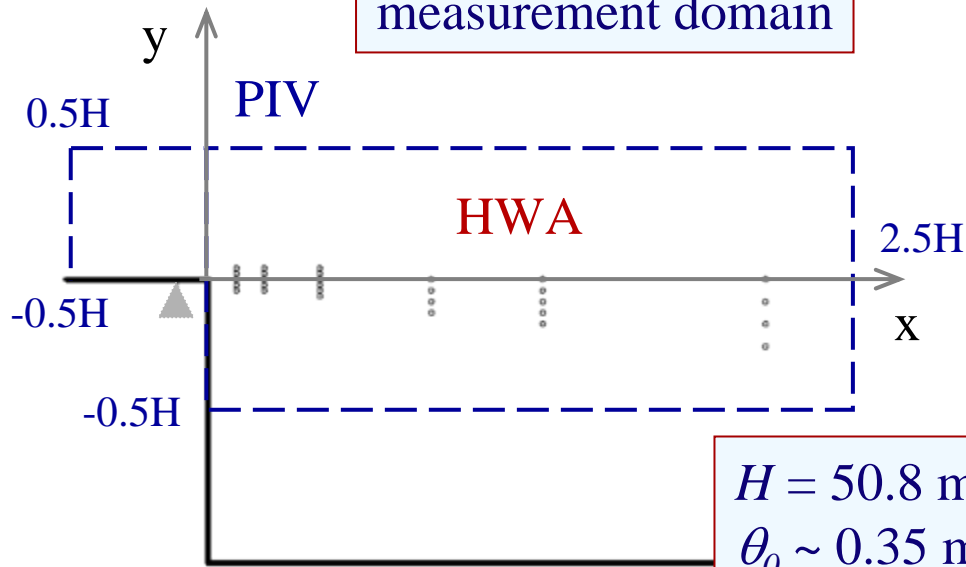
**Non Linear**

- Integrated numerically

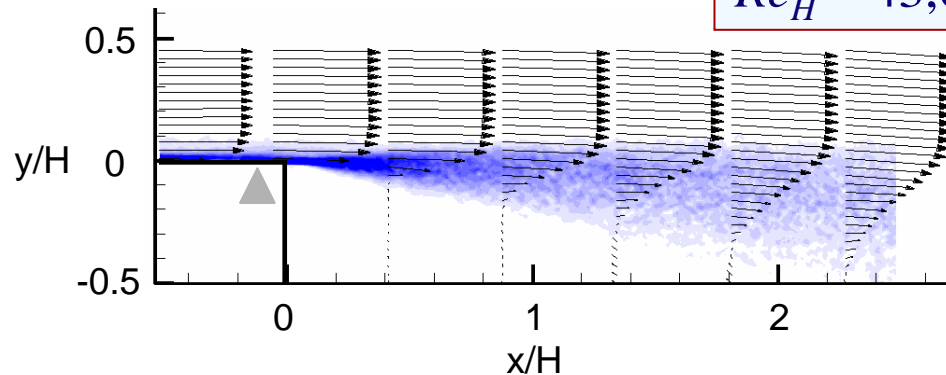
$$\left[ R_m^{i+1} \Delta x + Q_m^{i+1} \right] X_m^{i+1} = Q_m^{i+1} X_m^i + N_m^{i+1} \quad \text{where} \quad X^i = \left[ \dots \tilde{\chi}_m^i, \phi_m^i, \dots \right]^T$$

# The Unforced (Baseline) Flow

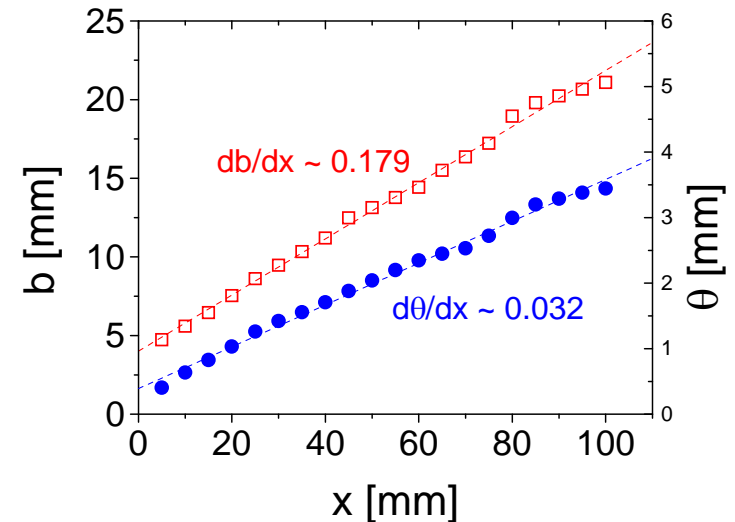
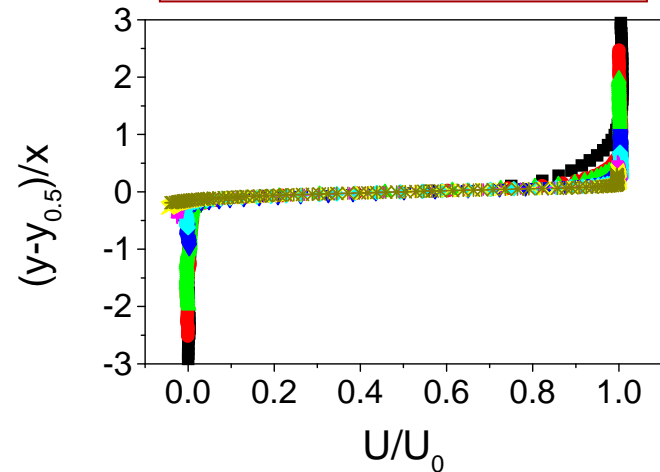
measurement domain



$H = 50.8 \text{ mm}$   
 $\theta_0 \sim 0.35 \text{ mm}$   
 $Re_{\theta_0} \sim 470$   
 $Re_H \sim 43,000$

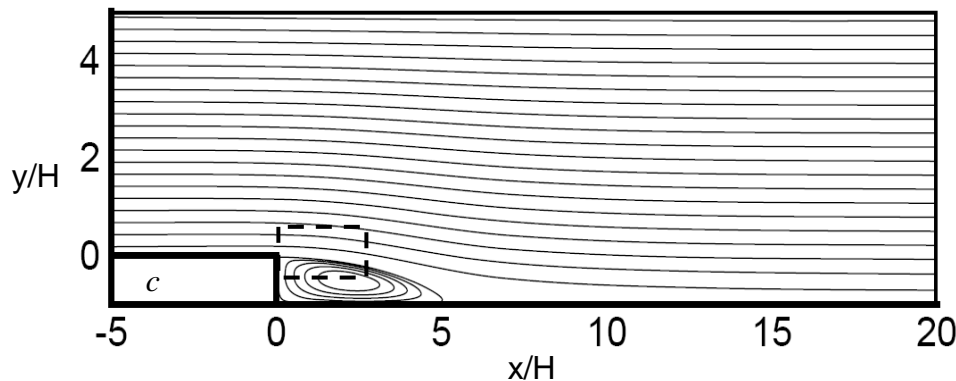
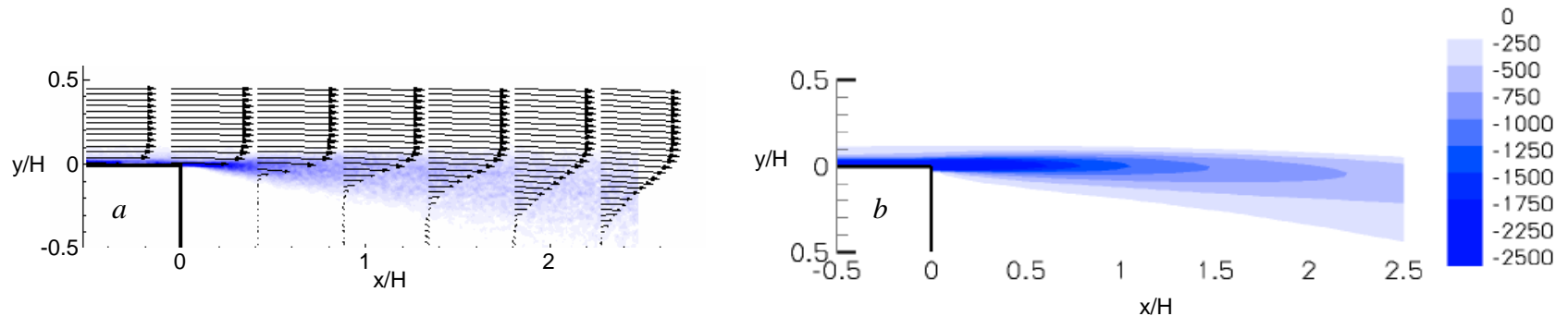


shear layer evolution



# Computed Baseline Flow

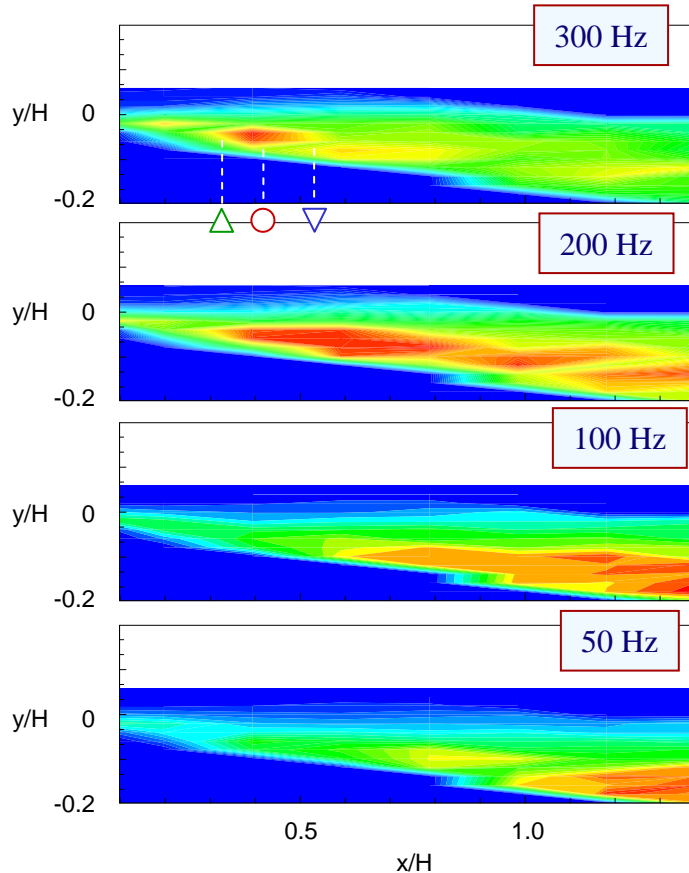
- Experimental baseline flow conditions matched within measurement domain



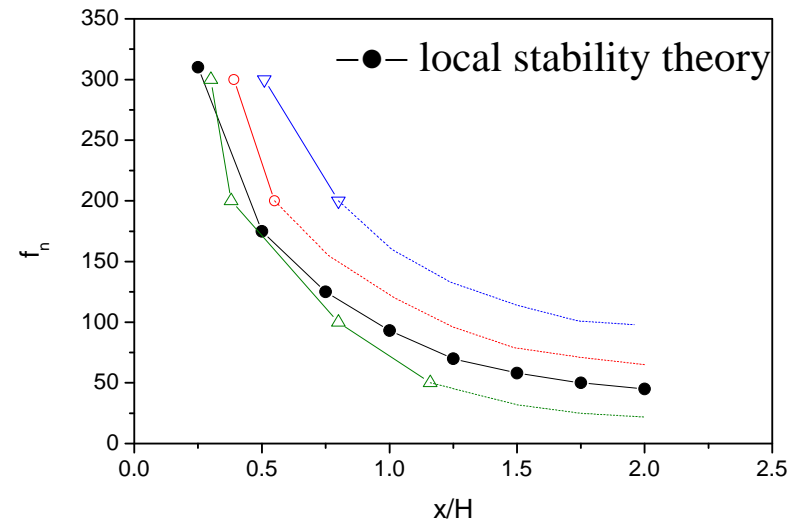
- Full computational domain:
  - Extended spatial domain
  - Reduced temporal domain

# The Unforced (Baseline) Flow

## EXPERIMENTAL: disturbance amplification



## ANALYTICAL: most amplified frequency



- The local natural frequency decreases along the expanding shear layer
- Agreement with experimental results of most amplified frequencies

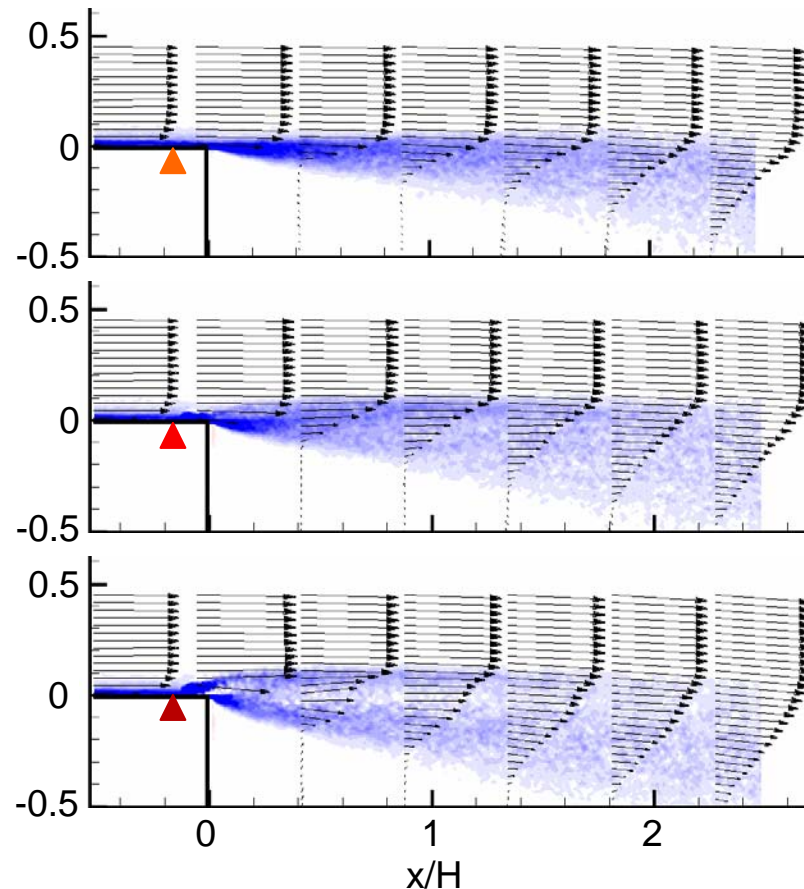
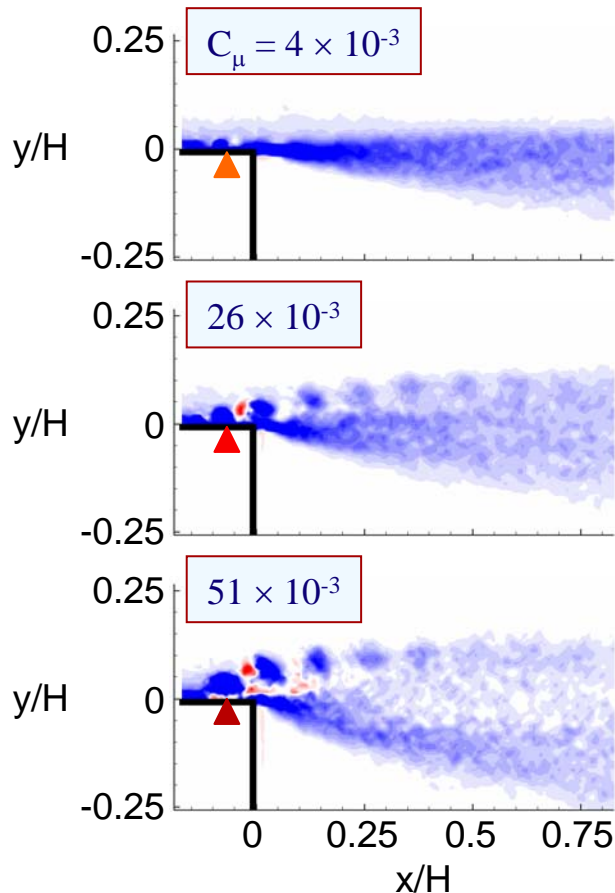


# Continuous High-frequency Actuation

- momentum coefficient  $C_\mu = \rho U_j^2 b_j / (\rho U_0^2 H)$

phase average

ensemble average



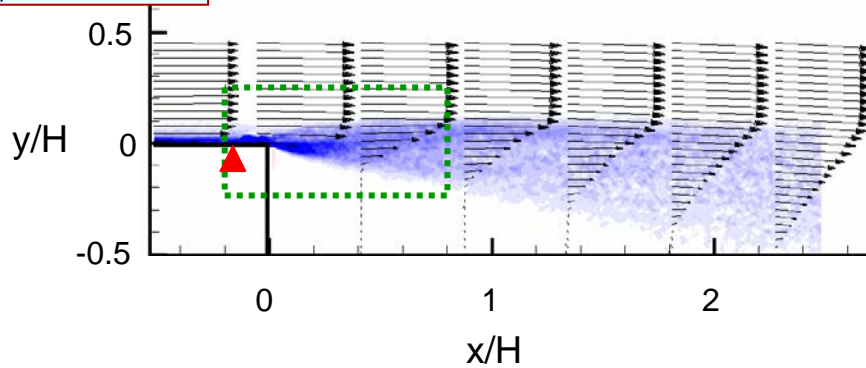


# Continuous High-Frequency Actuation

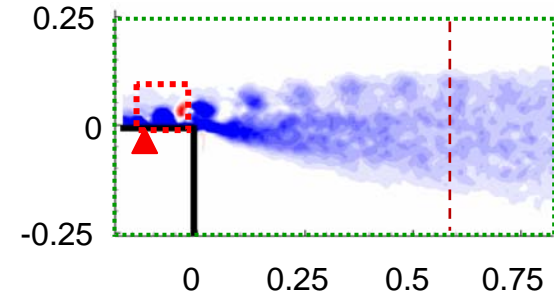
$$f = 2000 \text{ Hz}$$

$$C_{\mu} = 26 \times 10^{-3}$$

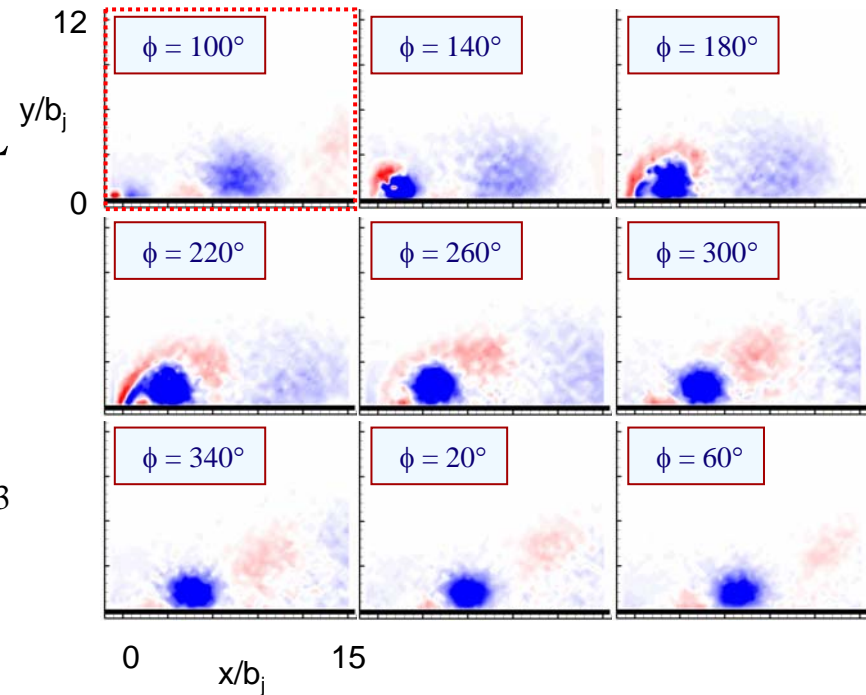
ensemble average



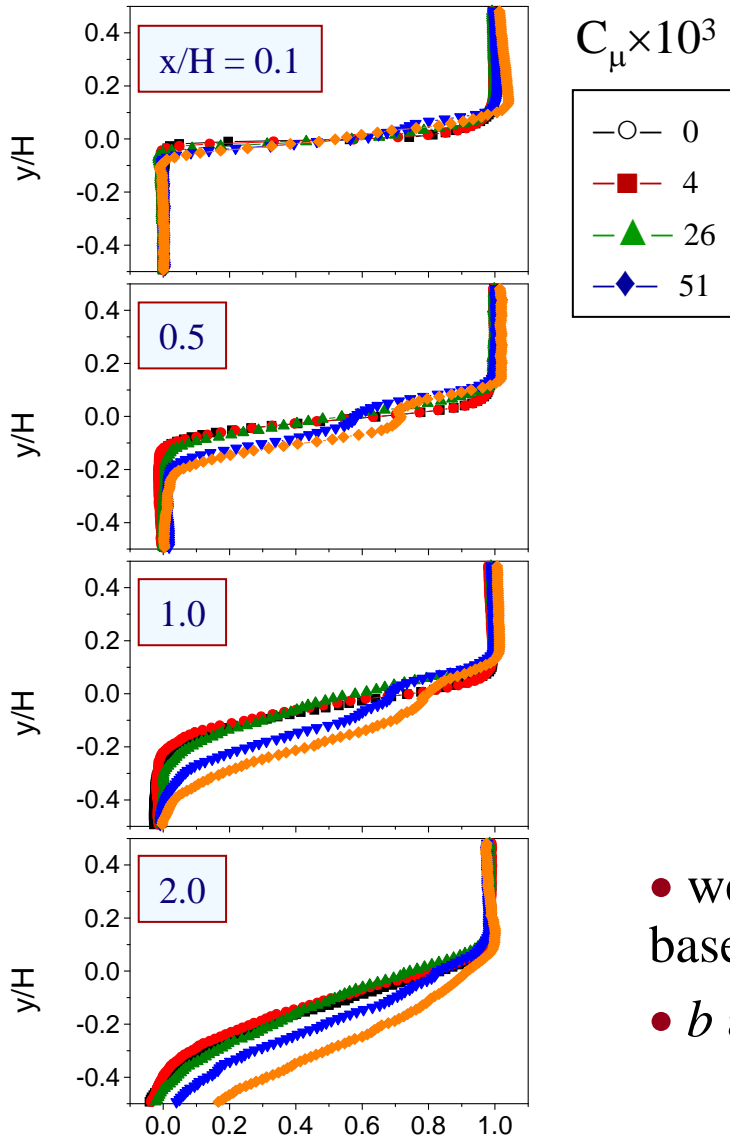
phase averaged



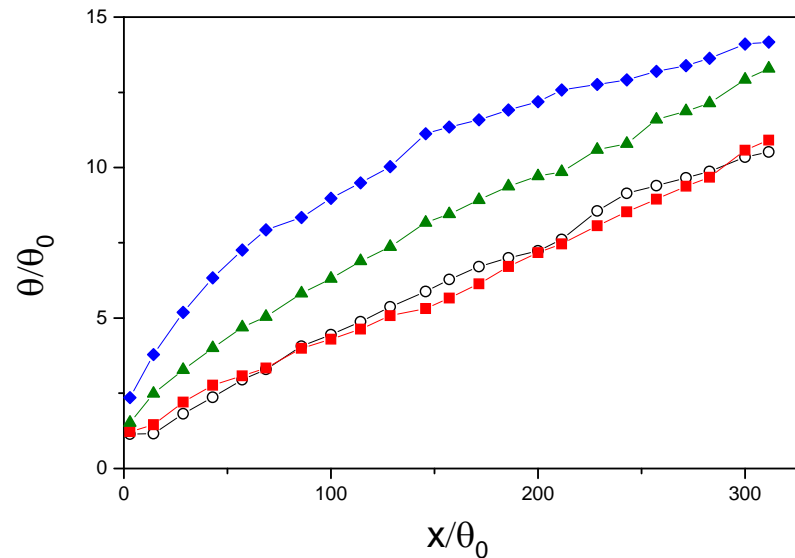
- Temporal and spatial alteration of the BL vorticity
- CCW vortex displaced and accelerated around CW vortex
- $f = 2000 \text{ Hz}$
- $C_{\mu} = \rho U_j^2 b_j / (\rho U_0^2 H) = 4, 26, 51, 69 \times 10^{-3}$



# Characterization of the Forced Shear Layer: Mean Flow



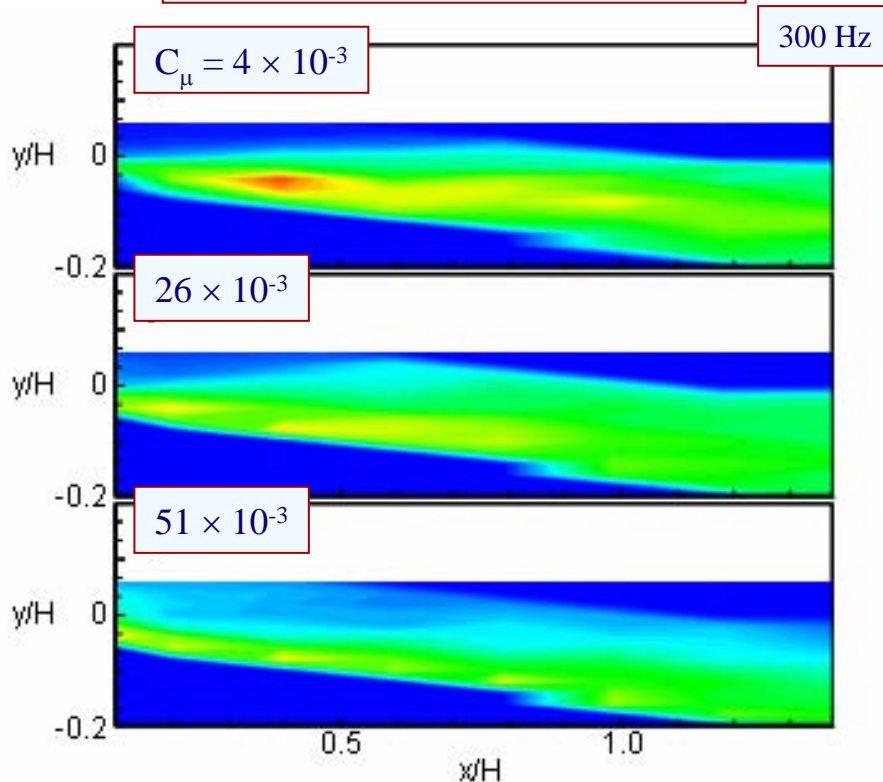
momentum thickness



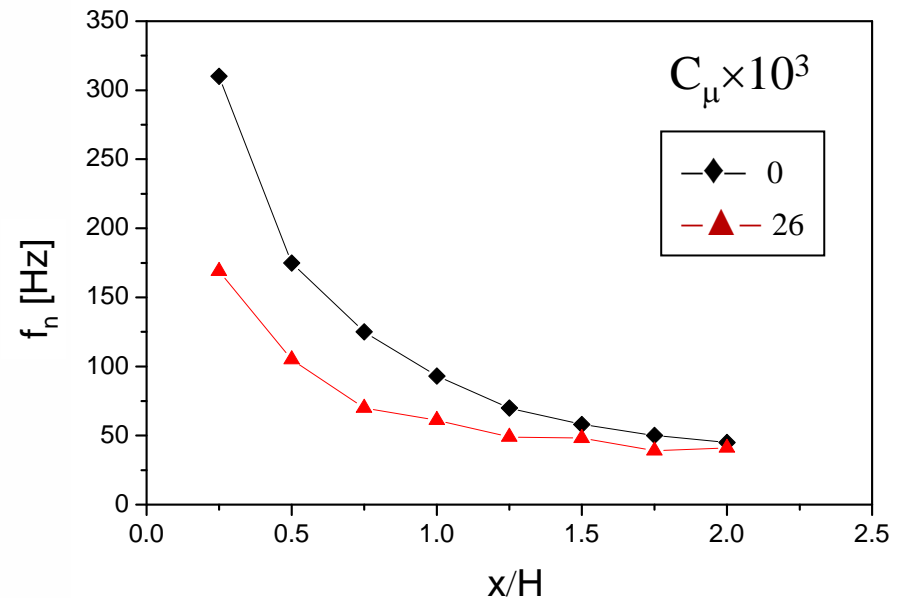
- weak forcing ( $C_\mu = 4 \times 10^{-3}$ ) does not alter the baseline flow
- $b$  and  $\theta$  increase with  $C_\mu$

# Characterization of the Forced Shear Layer: Natural Frequency

EXPERIMENTAL:  
disturbance amplification



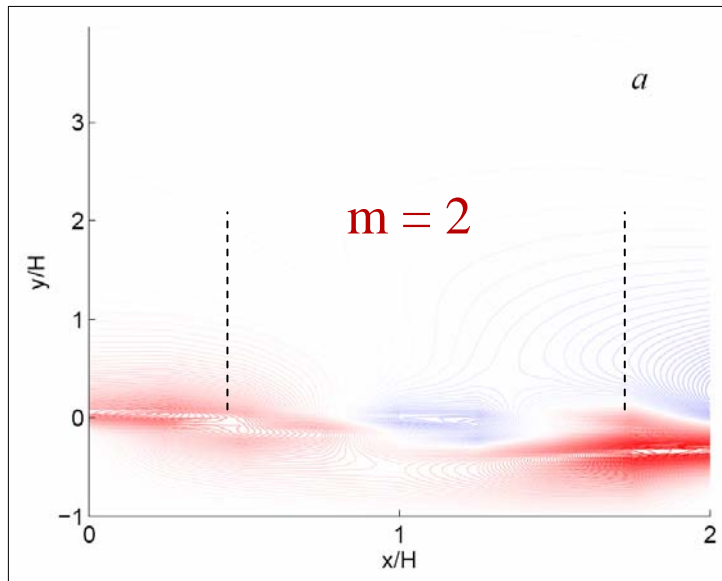
ANALYTICAL:  
most amplified frequency



- Local natural frequency lowered by the actuation
- Relates to the shear layer thickening

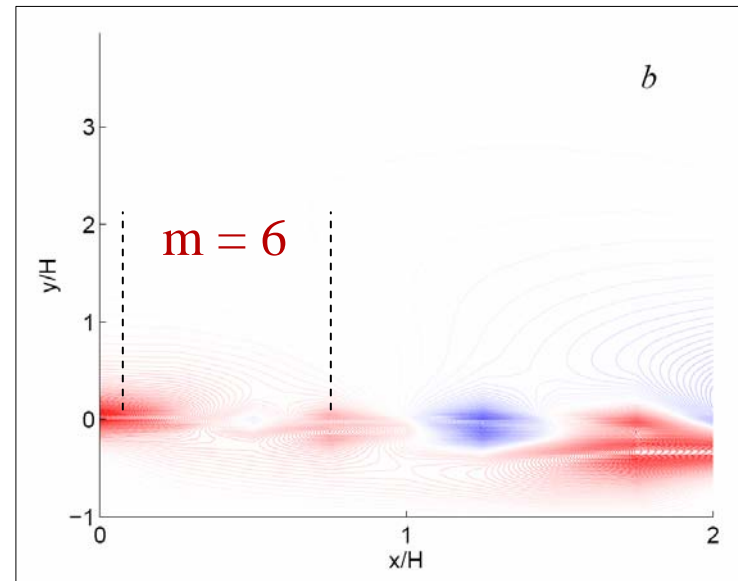
# NPSE Computed Flows

NO ACTUATION



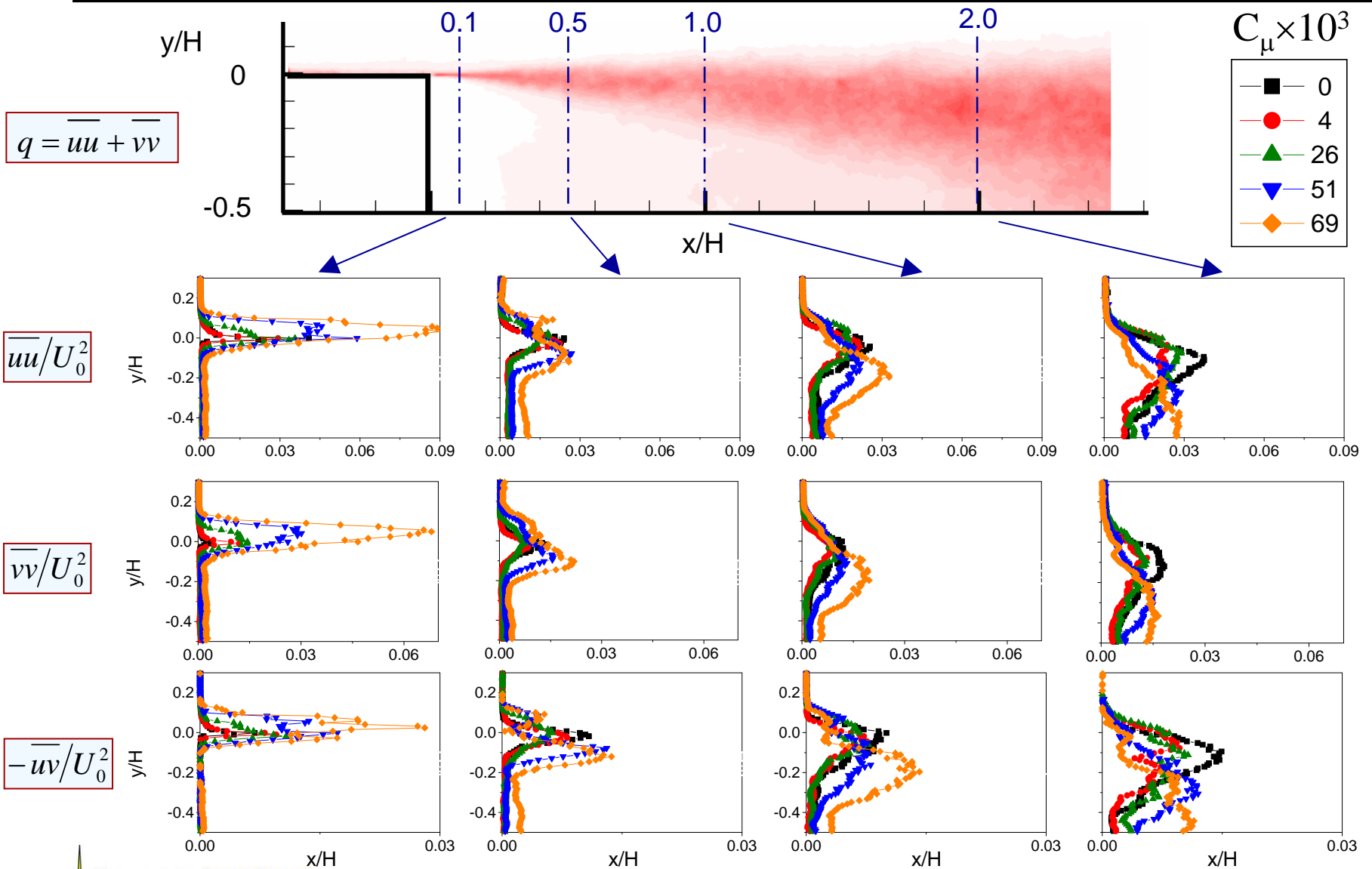
MODE 6 ACTUATION

$$St_H = 0.97$$



- NPSE calculation (6 modes are used): vorticity perturbations field is presented
- In the “natural” case (a), the low-frequency mode dominates
- In the “actuated” case (b) of increased amplitude of mode 6, high frequency mode dominates

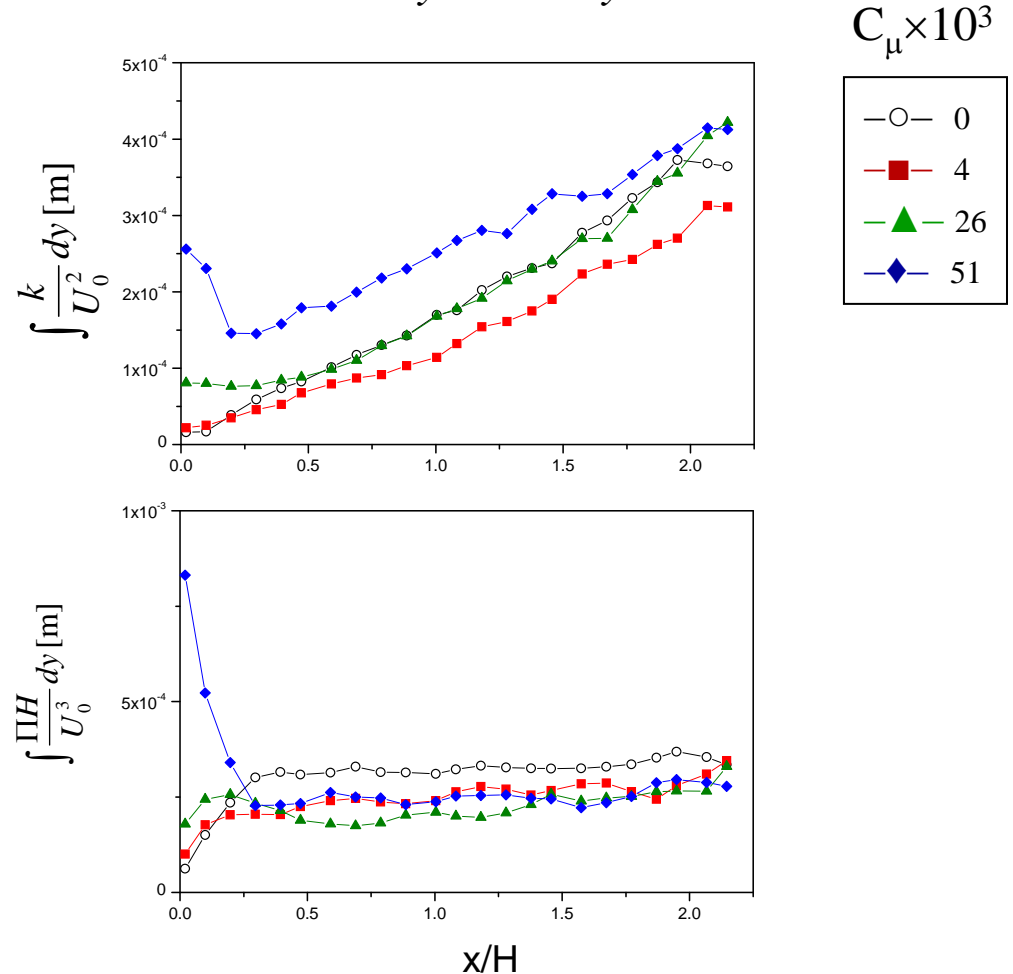
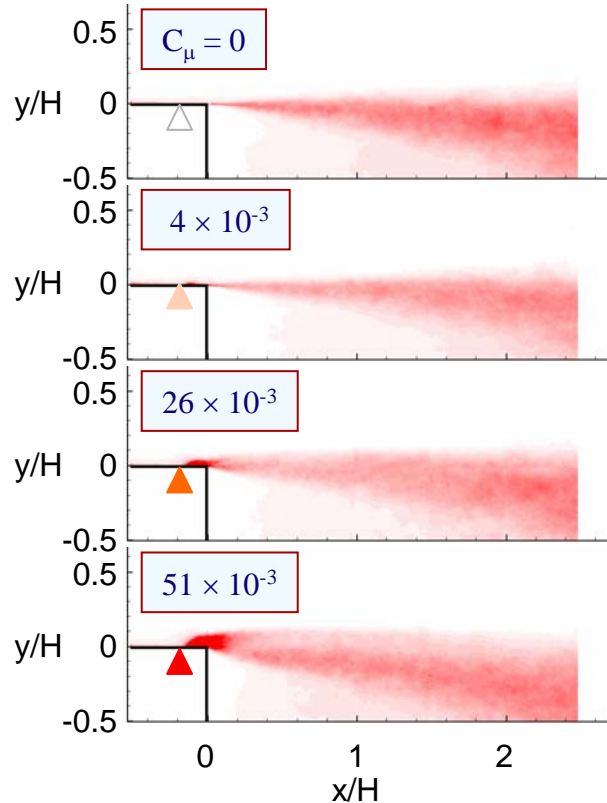
# Reynolds Stresses

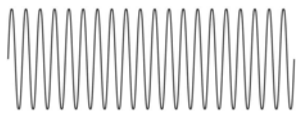


# Turbulent Kinetic Energy

$$q = \overline{uu} + \overline{vv}$$

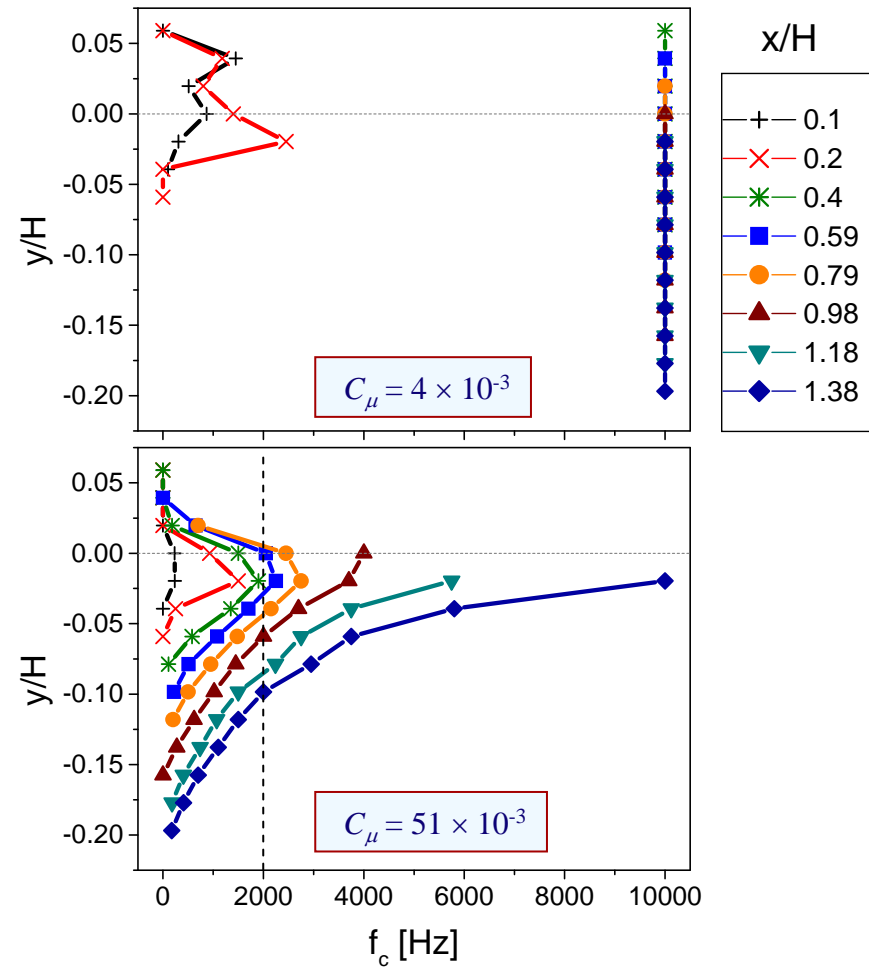
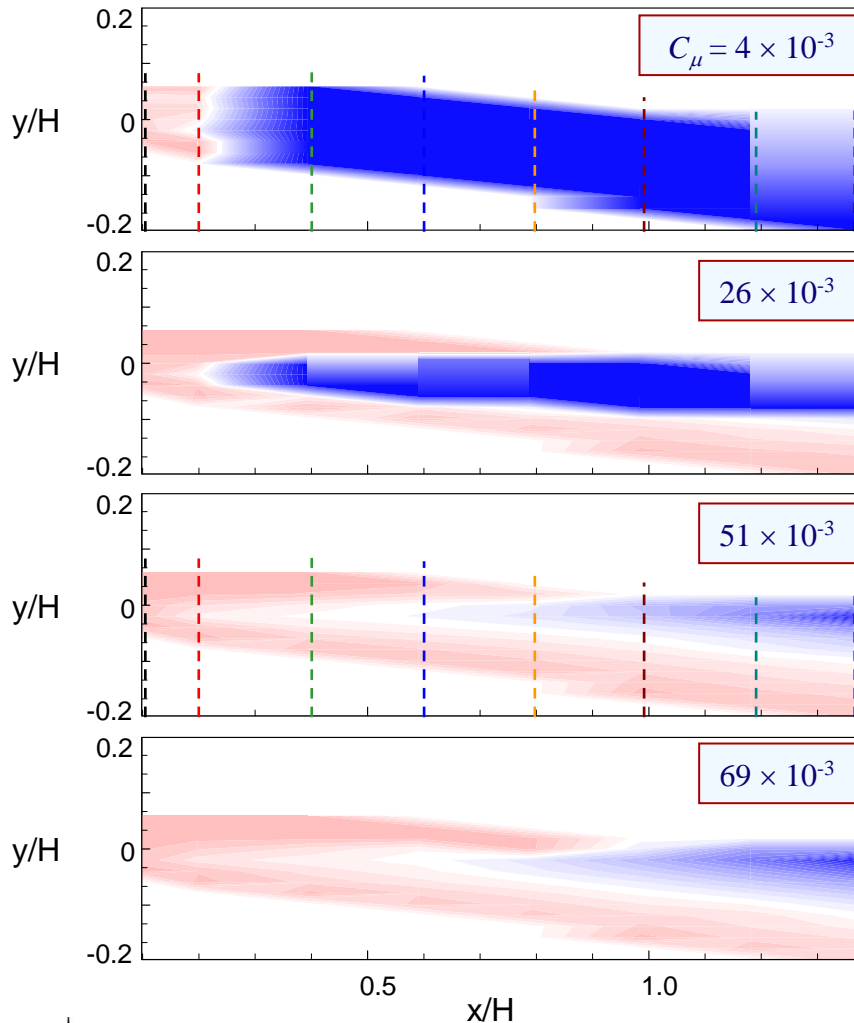
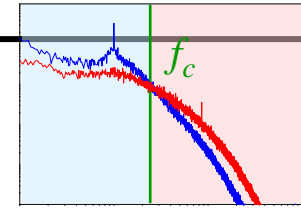
$$\Pi = -\overline{uu} \frac{\partial \overline{U}}{\partial x} - \overline{vv} \frac{\partial \overline{V}}{\partial y} - \overline{uv} \left( \frac{\partial \overline{U}}{\partial y} + \frac{\partial \overline{V}}{\partial x} \right)$$





# Energy Transfer: $St_H = 7.36$

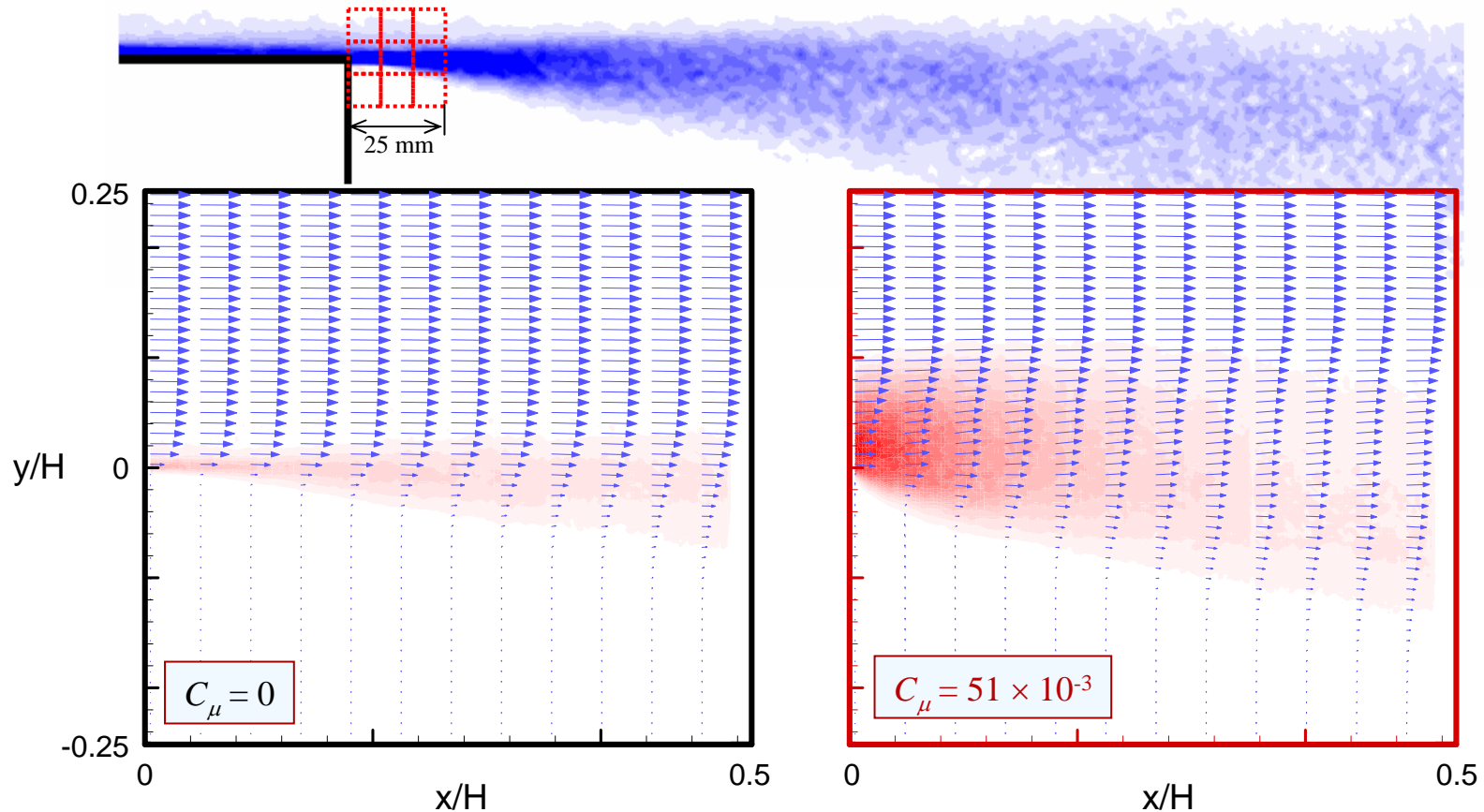
cross-over frequency  $f_c$





# Turbulent Dissipation Rate: $St_H = 7.36$

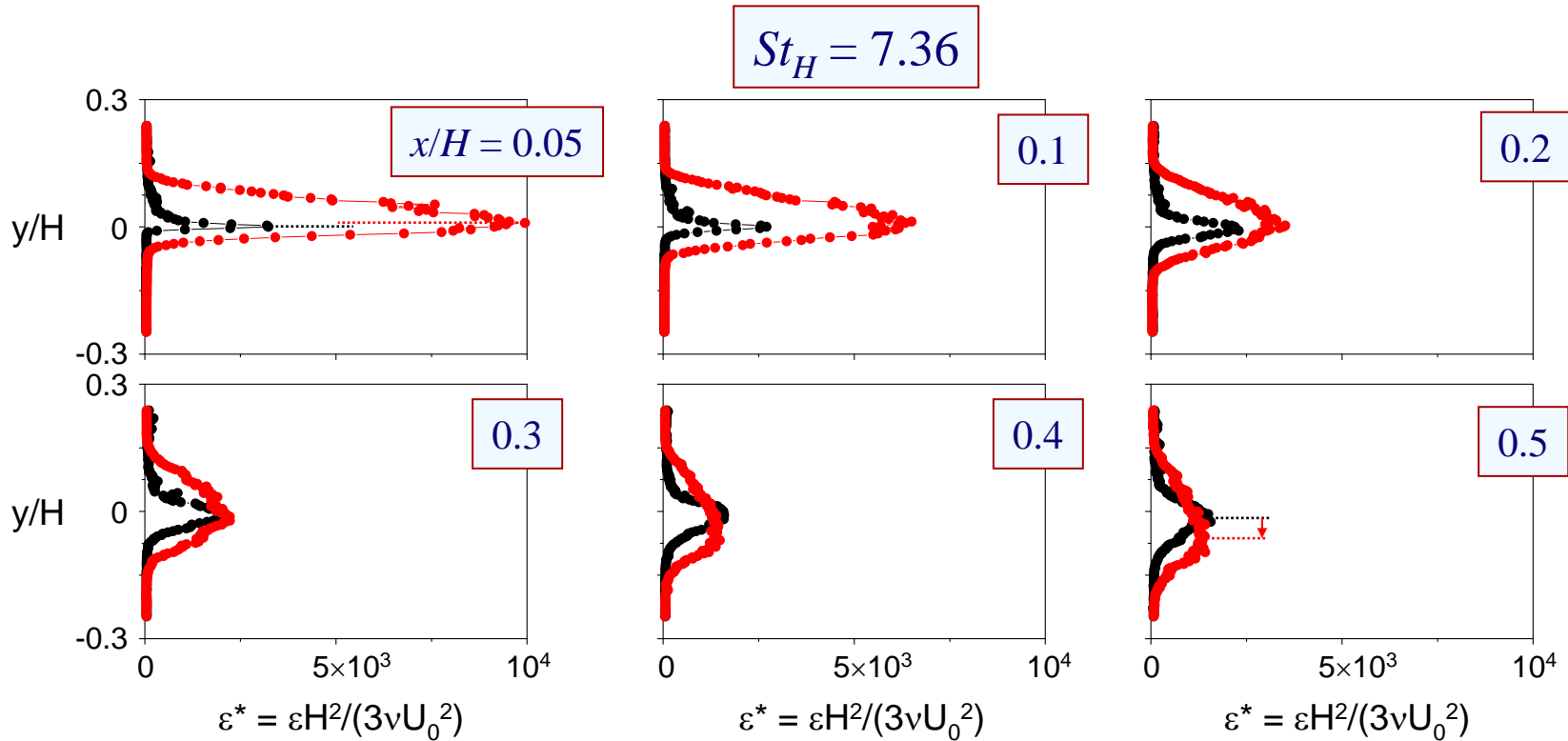
$$\varepsilon = 3\nu \left[ \overline{\left(\frac{\partial u}{\partial x}\right)^2} + \overline{\left(\frac{\partial v}{\partial y}\right)^2} + \overline{\left(\frac{\partial u}{\partial y}\right)^2} + \overline{\left(\frac{\partial v}{\partial x}\right)^2} + 2\overline{\left(\frac{\partial u}{\partial y} \frac{\partial v}{\partial x}\right)} + \frac{2}{3}\overline{\left(\frac{\partial u}{\partial x} \frac{\partial v}{\partial y}\right)} \right]$$



- Actuation leads to an *order of magnitude increase* in turbulent dissipation rate in the near field

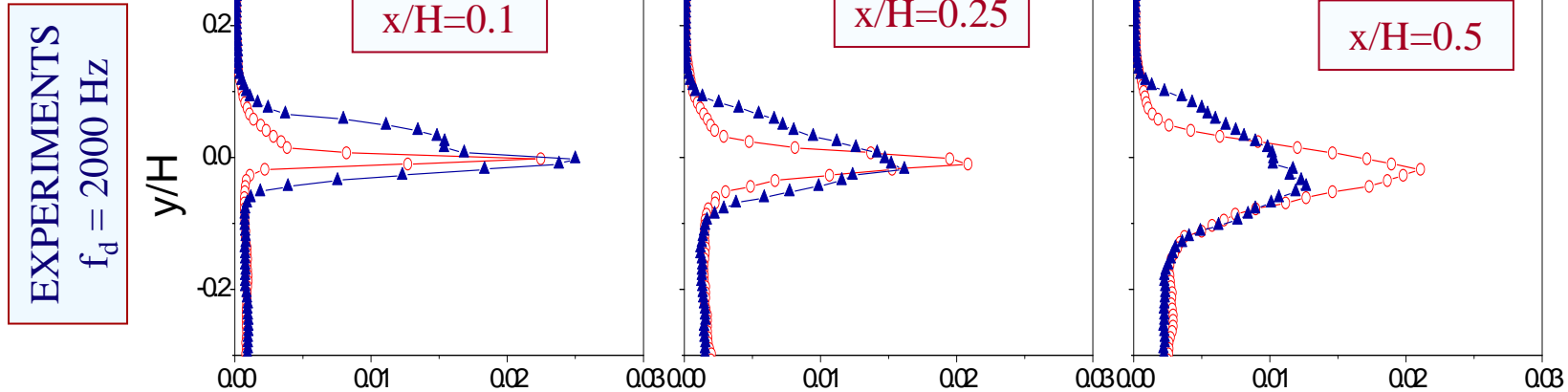


# Turbulent Dissipation Profiles

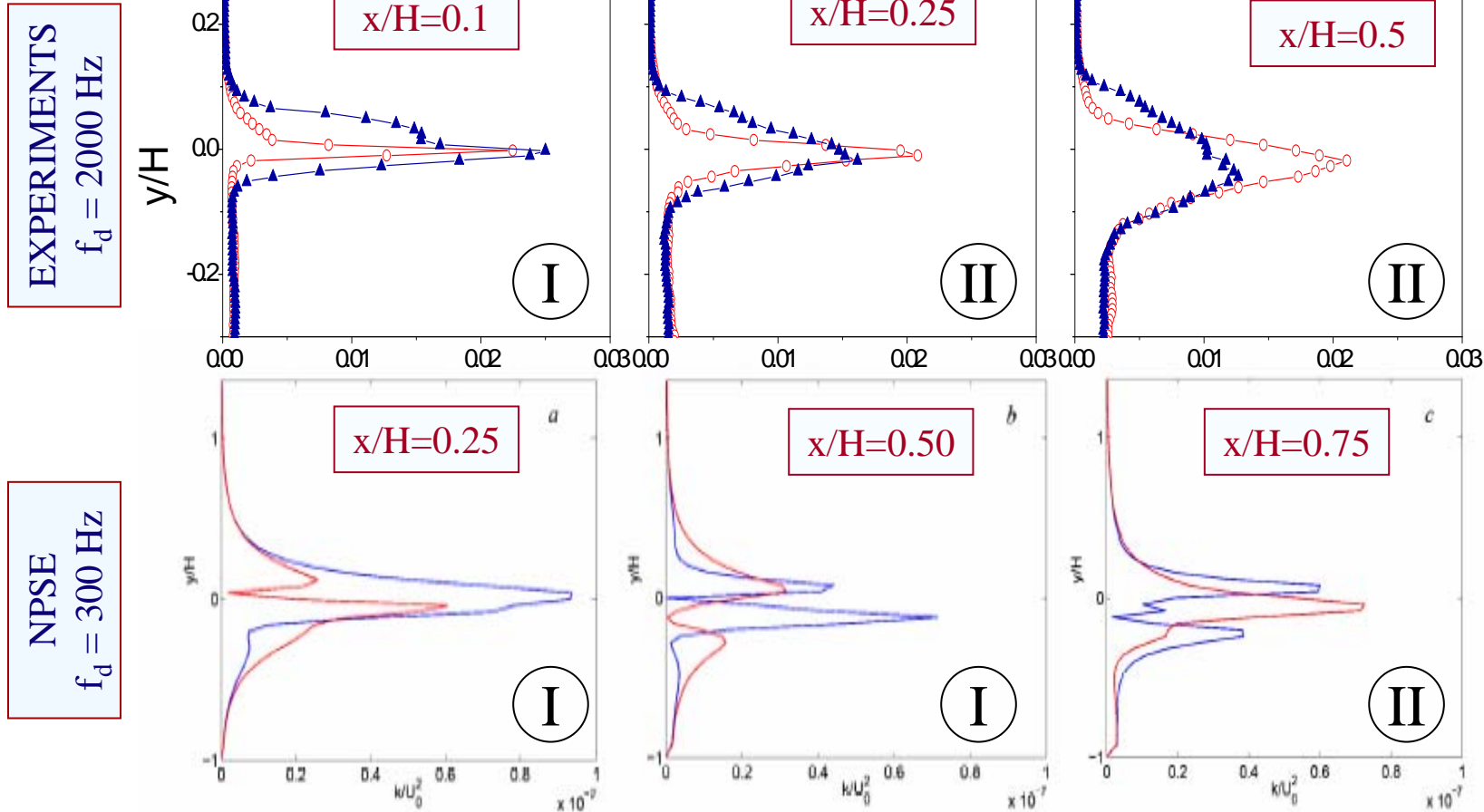


- **Baseline flow:** dissipation peak in the near-wall region. **Controlled flow:** much broader peak with an order of magnitude higher amplitude
- As the flow evolves, dissipation enhancement is reduced and becomes comparable to the unforced flow
- The controlled flow exhibits enhanced dissipation at shear layer edges

# Experimental TKE Profiles



# Experimental and NPSE TKE Profiles



I – small-scale structures dominate

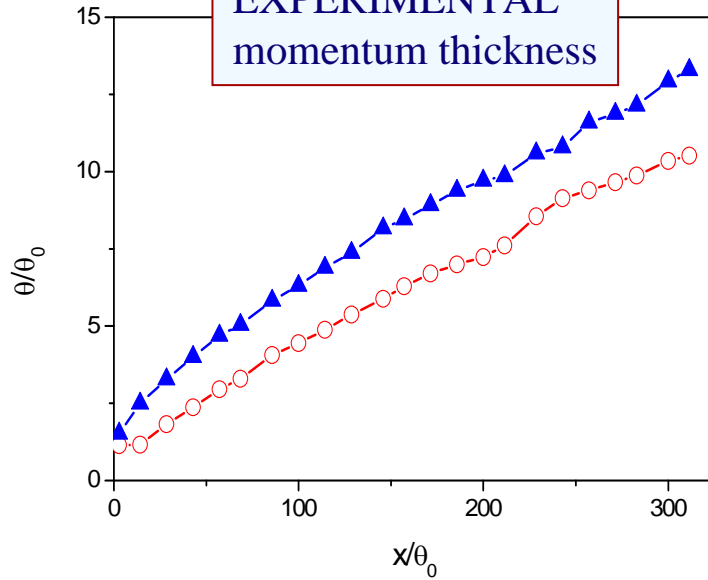
II – peak energy lowered and energy is broadened (thicker shear layer)



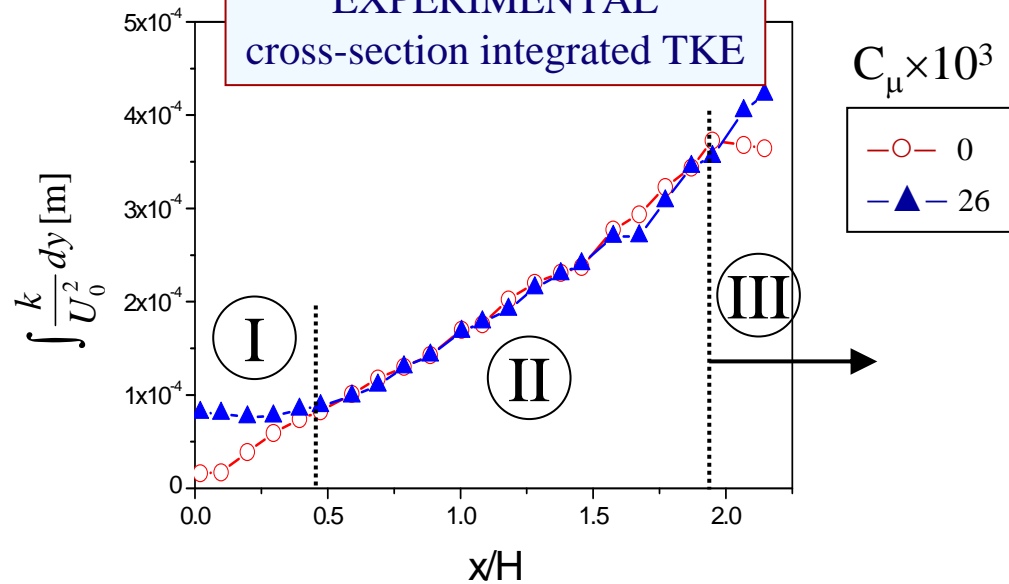
FlowCAD

# Regions of HF Influence

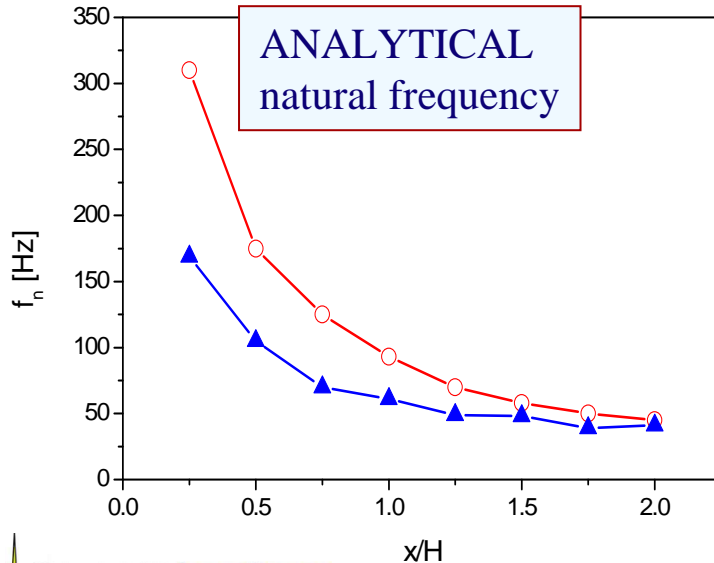
EXPERIMENTAL  
momentum thickness



EXPERIMENTAL  
cross-section integrated TKE

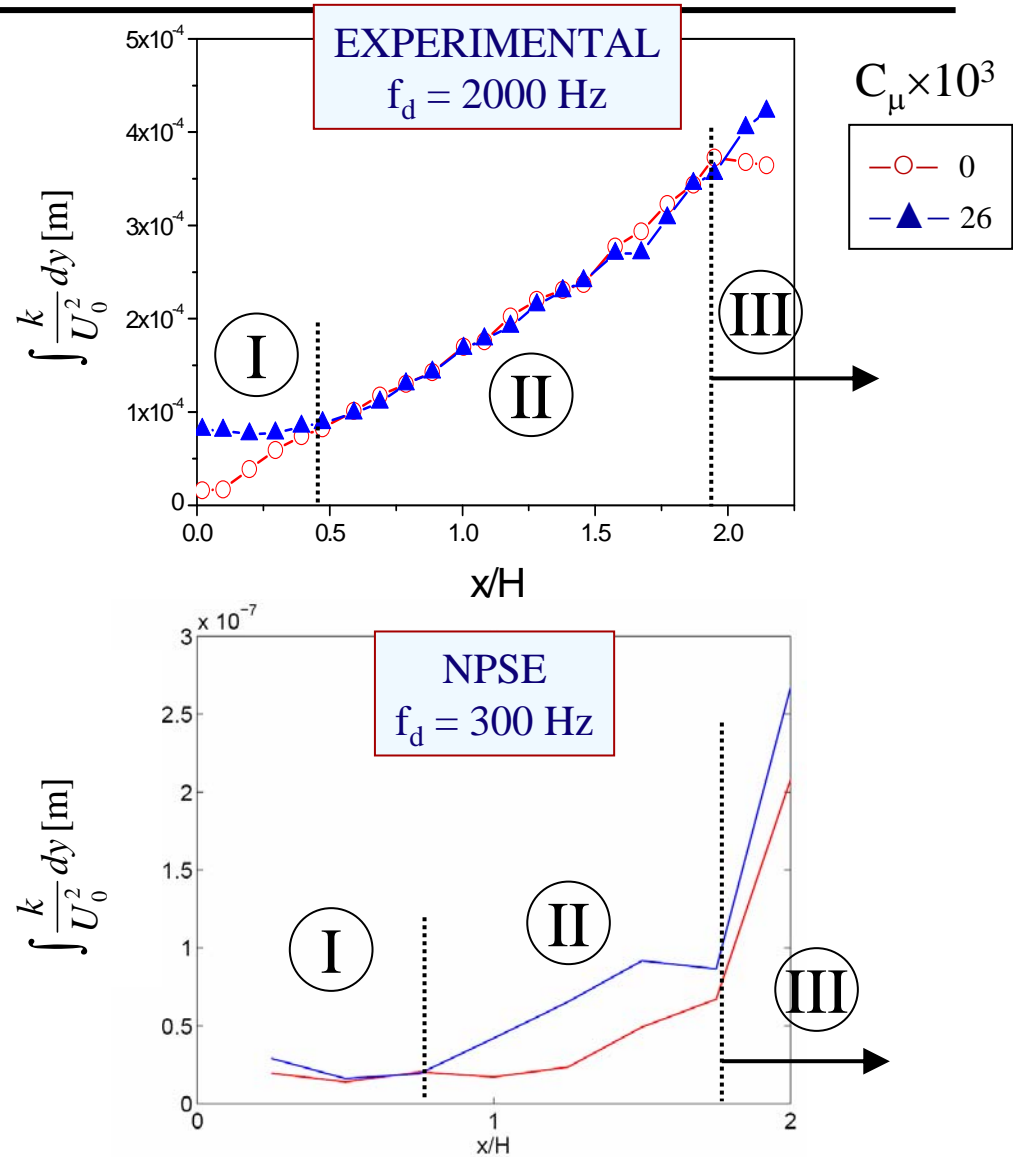


ANALYTICAL  
natural frequency



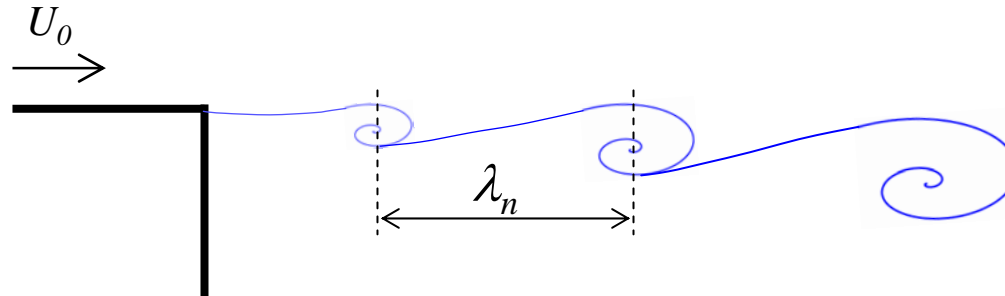
- Region I - actuation increases TKE
- Region II – actuation spreads TKE and reduces its peak in the thickened shear layer
- Region III - low frequency mode re-emerges

# Cross-sectional Integrated TKE

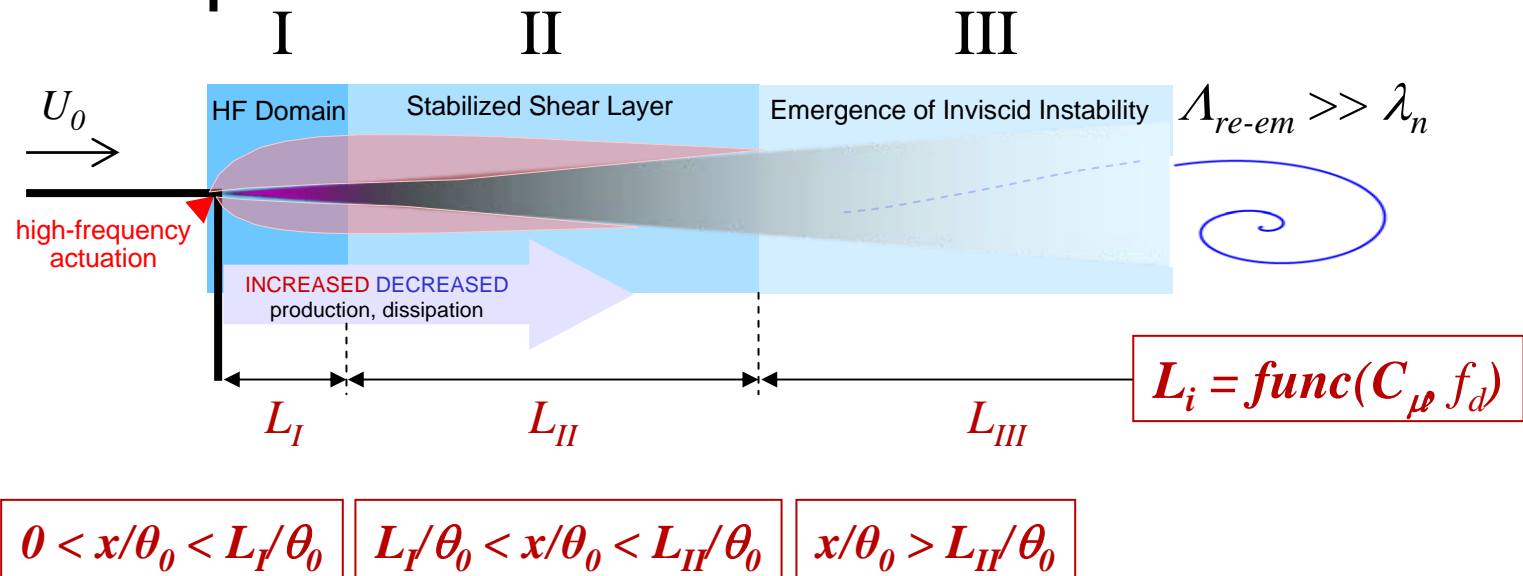


# High-Frequency Control

uncontrolled



controlled

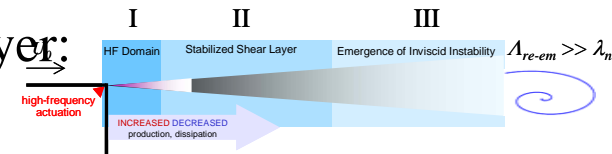


- Under HF actuation, three regions of shear layer are found



# Conclusions

- Direct small-scale manipulation of the BFS shear layer is investigated experimentally and numerically.
- Continuous high-frequency actuation is effected by interaction of a small-scale vortex train with the shear layer.
- Stability analysis suggests that high-frequency actuation is characterized by  $f_d > 2f_{n,max}$ .
- High-frequency actuation modifies the base shear layer:



- **Region I:**
  - much thicker shear layer and significantly lower natural frequencies
  - increase in both TKE production and dissipation
  - “stabilized” flow to fundamental instability
- **Region II:**
  - thicker shear layer and lower natural frequencies
  - suppressed peak of TKE and spread of energy in the thicker shear layer
  - “stabilized” flow to fundamental instability
- **Region III:**
  - Energy of high-frequency actuation is dissipated
  - No significant alteration of shear layer thickness and natural frequencies
  - Re-emergence of inviscid instability, but at lower frequency and spatially delayed

# Discussion: High-Frequency Excitation

- The possible mechanism:
  - high-frequency excitation of mode M modifies the mean flow through the zero mode changes
  - the modified mean flow interacts with the low frequency modes ( $\omega_1, \omega_2, \dots, 2\omega_{n,\max}$ ) to redistribute their energy and lower it

$M \& \text{conj}(M) \rightarrow 0 \rightarrow 0 \& 1 + 0 \& \text{conj}(1) \rightarrow \text{modified } 1;$   
 $\rightarrow 0 \& 2 + 0 \& \text{conj}(2) \rightarrow \text{modified } 2; \dots$

- As the strength of mode M decreases along the shear layer its effect decreases and low-frequency modes reappear but at lower natural frequencies